Two-Dimensional Drift-Diffusion Simulation of Organic Solar Cells

Christian Ahläng
34777
Master's Thesis
Åbo Akademi University
Faculty of Science and Engineering
Physics

February 2016

Abstract

The aim of this master's thesis is to develop a two-dimensional drift-diffusion model, which describes charge transport in organic solar cells. The main benefit of a two-dimensional model compared to a one-dimensional one is the inclusion of the nanoscale morphology of the active layer of a bulk heterojunction solar cell. The developed model was used to study recombination dynamics at the donor-acceptor interface. In some cases, it was possible to determine effective parameters, which reproduce the results of the two-dimensional model in the one-dimensional case.

A summary of the theory of charge transport in semiconductors was presented and discussed in the context of organic materials. Additionally, the normalization and discretization procedures required to find a numerical solution to the charge transport problem were outlined. The charge transport problem was solved by implementing an iterative scheme called successive over-relaxation. The obtained solution is given as position-dependent electric potential, free charge carrier concentrations and current densities in the active layer.

An interfacial layer, separating the pure phases, was introduced in order to describe charge dynamics occurring at the interface between the donor and acceptor. For simplicity, an effective generation of free charge carriers in the interfacial layer was implemented. The pure phases simply act as transport layers for the photogenerated charges.

Langevin recombination was assumed in the two-dimensional model and an analysis of the apparent recombination rate in the one-dimensional case is presented. The recombination rate in a two-dimensional model is seen to effectively look like reduced Langevin recombination at open circuit. Replicating the J-U curves obtained in the two-dimensional model is, however, not possible by introducing a constant reduction factor in the Langevin recombination rate.

The impact of an acceptor domain in the pure donor phase was investigated. Two cases were considered, one where the acceptor domain is isolated and another where it is connected to the bulk of the acceptor. A comparison to the case where no isolated domains exist was done in order to quantify the observed reduction in the photocurrent. The results show that all charges generated at the isolated domain are lost to recombination, but the domain does not have a major impact on charge transport.

Trap-assisted recombination at interfacial trap states was investigated, as well as the surface dipole caused by the trapped charges. A theoretical expression for the ideality factor n_{id} as a function of generation was derived and shown to agree with simulation data. When the theoretical expression was fitted to simulation data, no interface dipole was observed.

Abstrakt

Målet med denna pro gradu-avhandling var att utveckla en tvådimensionell drift–diffusion-simulering som lämpar sig för att beskriva laddningstransport i organiska solceller. Fördelen med en tvådimensionell modell jämfört med de endimensionella modellerna som normalt används är att morfologin i det aktiva lagret för en bulkgränsytesolcell kan tas i beaktande. Modellen som utvecklades användes följaktligen för att studera rekombination som inträffar vid gränsytor mellan det elektrondonerande och elektronaccepterande materialet.

Teorin bakom laddningstransport i halvledare presenterades och diskuterades med organiska material som utgångspunkt. En översikt av den normalisering och diskretisering av ekvationer som är nödvändig för att numeriskt kunna lösa ekvationerna som beskriver laddningstransporten introducerades. Numeriska lösningar erhölls med hjälp av en iterativ överrelaxationsmetod. Lösningen ges i form av positionsberoende elektrisk potential, laddningskoncentrationer och strömtäthet.

Ett gränsskikt som skiljer de två materialen åt implementerades för att beskriva gränsytan och de former av växelverkan som sker där. För enkelhetens skull implementerades fotogenerationen så att fria laddningar genereras vid gränsytan. De rena faserna av de två materialen fungerar endast som transportskikt för de fotogenererade laddningarna.

Den bimolekylära rekombinationshastigheten i den tvådimensionella modellen antogs ges av Langevin-rekombinationshastigheten och jämfördes med en endimensionell modell. Rekombinationshastigheten i den endimensionella modellen anpassades så att samma värde för V_{oc} erhölls som det i den tvådimensionella modellen. Rekombinationen i den tvådimensionella modellen visades då se ut som reducerad Langevin-rekombination och ett uttryck för reduktionsfaktorn γ föreslogs.

Förlusten av fotogenererade laddningar förorsakad av isolerade domäner studerades genom att placera en acceptordomän i den rena donorfasen. Därefter studerades de två fall där domänen varit i kontakt med resten av acceptorfasen och det då domänen var helt isolerad. En stor minskning i fotoströmmen observerades och för att kvantifiera minskningen jämfördes de två fallen med det där domänen avlägsnades helt. Resultaten visar att alla laddningsbärare som genereras vid isolerade faser förloras genom rekombination.

Därtill undersöktes rekombination via fällor belägna vid gränsytan mellan donorn och acceptorn, samt den dipol som förorsakas av de fångade laddningarna. Ett teoretiskt uttryck för idealitetsfaktorn n_{id} härleddes och visades stämma väl överens med de simulerade värdena för V_{oc}. Då en kurvanpassning av uttrycket till de simulerade värdena gjordes kunde ingen inverkan av dipolen observeras.

Förord

Efter att ha bekantat mig med organiska halvledare i laboratoriet såg jag fram emot att få göra mer teoretiskt arbete inom det intressanta fältet. Då professor Ronald Österbacka föreslog att jag kunde skriva min pro gradu-avhandling om simulering av organiska solceller tog jag glatt emot utmaningen. Under arbetets gång har jag lärt mig mycket och upplevt otaliga insikter inom det komplicerade området. Därtill fick jag en orsak att sätta mig in i grundläggande programmering som sannolikt kommer att vara en viktig kunskap i framtiden.

Jag vill tacka mina handledare Ronald Österbacka och Oskar Sandberg för många givande och lärorika diskussioner. Därtill har också Markus Lindberg bidragit med många insiktsfulla kommentarer. Även debatterna med studiekamrater under de gångna åren har lett till en djupare förståelse av många viktiga fenomen.

Christian Ahläng
Åbo, februari 2016

Contents

Chapter 1

Introduction

Organic solar cells, usually classified as a group of emerging photovoltaic devices, have shown a tremendous increase in efficiency during the last decade. Organic photovoltaics are, however, still far from the efficiencies reached by their inorganic counterparts. The lower efficiency is a result of large energy barrier for dissociation of generated charges and lower mobilities, causing increased recombination [1]. A better understanding of the recombination processes that occur in the materials and tuning of properties such as the band gap are essential to further improve the efficiency of organic photovoltaic devices.

The aim of this work is to develop a two-dimensional drift-diffusion model for organic solar cells. In order to create an accurate model a good understanding of charge transport dynamics is required. The underlying theory utilized in developing the model is outlined in chapters 2 and 3. To ensure the viability of the model some basic theoretical predictions have been replicated. The main goal of the simulations that have been carried out is to determine the impact of recombination in an organic solar cell.

Models like the one developed in this work are useful tools for replicating and describing observed behaviors of a system. Simulations can also be utilized when trying to optimize a set of parameters for a system. This way time-consuming trial and error in a laboratory can be avoided.

Chapter 2

Organic Semiconductors

In this chapter, a general description of organic semiconductors will be presented, as well as an introduction to organic photovoltaics. The aim of this chapter is to give the reader the necessary background information on the sometimes vastly different properties of organic materials compared to the more common, inorganic semiconductors.

2.1 Electronic Properties

Organic materials exhibit quite different properties compared to inorganic crystals. The inherent disorder and weak binding forces encountered in organic materials lead to completely different charge transport properties. A basic understanding of the energy structure found in organic materials can be obtained by considering the transition from a single molecule to a molecular solid.

2.1.1 Molecular Properties

Rings or chains of carbon atoms bound together by alternating single and double bonds are called conjugated segments. Conjugated hydrocarbon molecules, which are some of the simplest organic molecules, are made up of one or more of these

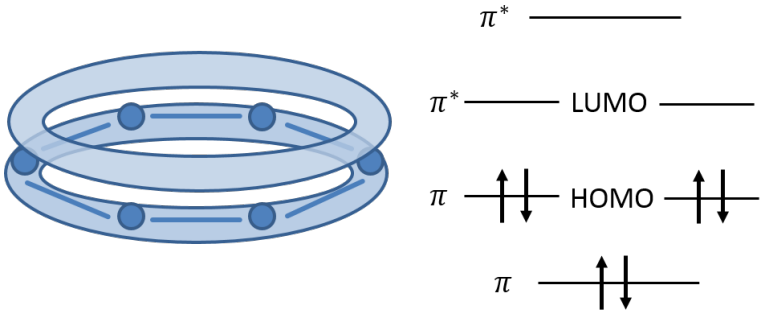

Figure 2.1: Schematic picture of the delocalized π-orbitals of a benzene molecule. The π-bonds can be seen as three energy levels that extend over the whole ring structure. The energy levels are also presented on an energy scale showing the ground state where the π-bonds are fully occupied. The π^*-binding energies correspond to excited states of the molecule.

conjugated segments. The electrons that participate in the double bonds are called π-electrons and are delocalized over the conjugated segment. In benzene, a simple aromatic hydrocarbon molecule, the six π-electrons are delocalized over the whole molecule and occupy three molecular orbitals. The highest occupied molecular orbital (HOMO) and the lowest unoccupied molecular orbital (LUMO) are of special importance, as electronic transitions mainly take place between these levels. In Figure 2.1, the delocalized π-orbitals and molecular orbitals of benzene are shown.

2.1.2 Molecular Solids

The materials used in bulk heterojunction solar cells are generally amorphous, meaning that no long range order exists in the solid. The inherent disorder is a result of the weak van der Waals forces that bind neighboring molecules together, thus forming a solid. The disorder is seen as variation in intermolecular distances and relative orientation of the molecules among other things. The energy levels of the molecular orbitals are shifted from the single-molecule value when a solid is formed. The shift of the energy levels depends on intermolecular distance and orientation of neighboring molecules and, therefore, a broad density of states is observed in the materials. The HOMO and LUMO levels in the solid commonly exhibit a Gaussian density of states [2]. Electrons and holes are transported at these broad levels, made up of isolated states. For simplicity, the terms conduction band E_C and valence band E_V will be used to describe the energy levels at which electrons and holes are transported, even though no continuous bands exist in disordered organic semiconductors.

Upon photoexcitation, an electron is excited to a higher lying state and a hole is left behind at the state previously occupied by the electron. The electron and hole remain coulombically bound and can be described as an exciton, having no net charge. The binding energy of the exciton is on the order of 300 meV, meaning that spontaneous dissociation is very unlikely. A schematic picture of the energy levels of the bound electron and holes is shown in Figure 2.2. Excitons are short-lived with a lifetime of about 1 ns after which the bound electron and hole recombine. Excitons are able to hop between molecules and typically diffuse 10 nm during their lifetime.

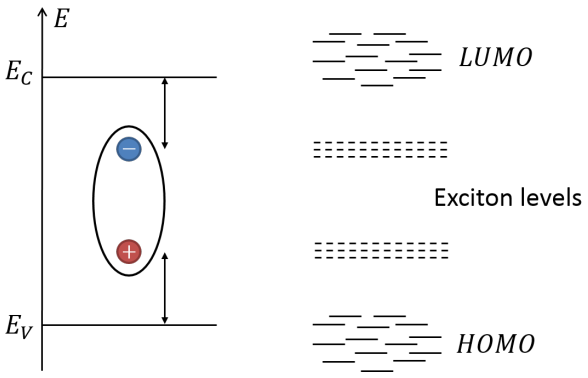

Figure 2.2: Schematic picture showing the energy levels of the bound electron-hole pair. The binding energy is the energy difference between the electron and E_C plus the energy difference between the hole and E_V, shown by the black arrows. To the right the HOMO and LUMO levels in the solid are shown as a reference to the simplified single-level model.

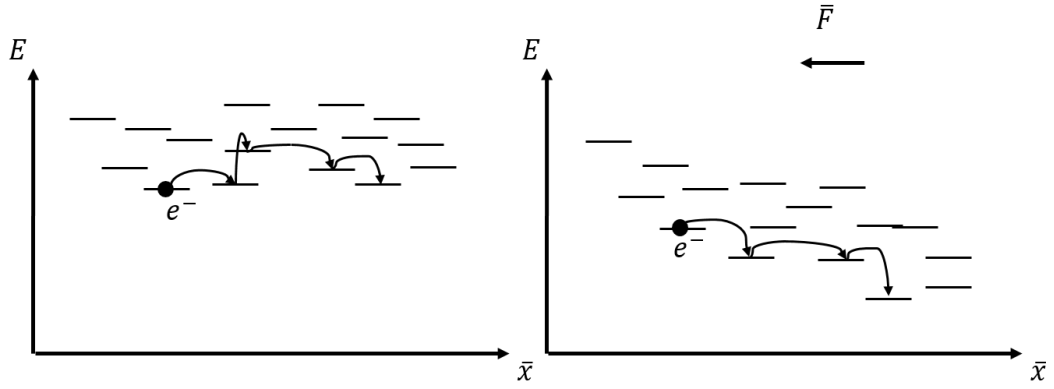

Figure 2.3: Schematic pictures of hopping transport in organic semiconductors with and without an electric field. Jumps to higher energies and over large distances are unlikely and limit the transport. An electric field increases the likelihood of finding nearby states with lower energy, thus increasing the mobility at low temperatures.

2.1.3 Hopping Transport

Free charge carriers in disordered organic materials are delocalized along conjugated segments but remain localized on these segments. Hopping transport is the term used to describe transport between the localized states, consisting of a series of tunneling events between the states. An expression for the hopping rate ν has been derived by R. Marcus [3], but in practice it is very difficult to calculate the hopping rate. Instead, the simpler Miller-Abrahams hopping rate is generally used [4]. The expression for the Miller-Abrahams hopping rate defines a maximum hopping rate ν_0 and then considers how it is reduced by spatial and energetic differences between states. The hopping rate from a state with energy E_i to another with energy E_j, separated by a distance R_{ij} is given by ν_{ij},

$$\nu_{ij} = \begin{cases} \nu_0 \exp\left(-\frac{R_{ij}}{\gamma}\right) \exp\left(-\frac{\Delta E_{ij}}{kT}\right) & \text{if } E_i < E_j \\ \nu_0 \exp\left(-\frac{R_{ij}}{\gamma}\right) & \text{if } E_i > E_j. \end{cases} \tag{2.1}$$

Here $\Delta E_{ij} = E_j - E_i$ is the difference in energy between the states, a hop to a state with lower energy is only affected by the distance between the states R_{ij}. The parameter γ is the localization radius, which is a measure of the wavefunction overlap between two states.

The transport in organic semiconductors is thermally activated as described by the Miller-Abrahams expression. An electric field F may also contribute to the mobility by ensuring that lower lying states are found nearby. An empirical expression for the field and temperature dependent mobility has been obtained from Monte Carlo simulations and shown to agree well with experiments [2]:

$$\mu(F,T) = \mu_0 \exp\left[-\left(\frac{2}{3}\frac{\sigma}{kT}\right)\right] \exp\left[CF^{1/2}\left(\left(\frac{\sigma}{kT}\right)^2 - \Sigma^2\right)\right]. \tag{2.2}$$

Here σ is the width of the Gaussian density of states, μ_0 is a material-dependent parameter and both C and Σ are empirical parameters fitted to experiments. The hopping transport of an electron at the LUMO level in the presence of an electric field is illustrated in Figure 2.3. In Figure 2.4, the mobility given in equation 2.2 is shown as a function $F^{1/2}$ for a number of temperatures. At room temperature the

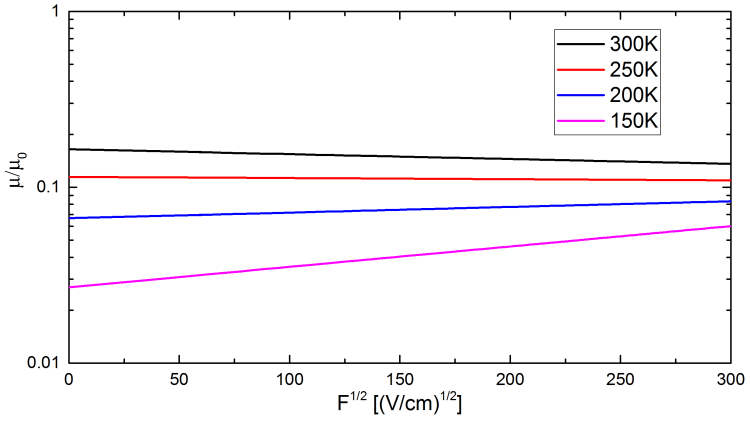

Figure 2.4: Mobility of P3HT as a function of $F^{1/2}$ for a number of temperatures. The mobility at room temperature is seen to be only weakly dependent on the electric field. The values for C and Σ are taken from [5].

mobility is only weakly dependent on the electric field, as seen in the figure and can therefore be assumed to be constant.

2.2 Organic Solar Cells

2.2.1 Working Principles of a Solar Cell

A solar cell produces energy by converting absorbed photons into free charge carriers, which can subsequently be extracted as electric current. The charges are extracted at electrodes, between which the active layer is sandwiched. The built-in potential V_{bi} is equal to the difference in work functions of the electrodes and the built-in field $\bar{F}_{\text{bi}} = -\nabla V_{\text{bi}}$ acts as a driving force in the solar cell by extracting photogenerated charges.

In this thesis, the difference in electrochemical potential between the electrodes is denoted U, while specific values of the potential difference are denoted by V. Similarly, currents will be denoted with a capital letter, J, while current densities are given a lower case letter, j. Power can be extracted from the solar cell when a potential difference U exists between the electrodes and the power output of the solar cell is given by $P = J \cdot U$. At dark conditions the solar cell behaves like a diode and a current J_{dark} flows through the device when a potential is applied.

Under illumination the total current J_{illu} is given by the sum of the dark current and the photocurrent J_{photo}, which is the current produced by photogenerated charges. The photocurrent can be approximated by assuming that the maximum drift-distance a charge travels is given by $l = \mu F \tau$ where τ is the lifetime of a free charge carrier. The photocurrent can then be calculated from the amount of charge which reaches the electrodes and can be extracted [6]. The following expressions are then obtained with the maximum value for the photocurrent density j_{photo} when l is larger than the thickness d of the active layer:

$$|j_{photo}| = \begin{cases} eG\mu\tau|V_{\text{bi}} - U|/d & \text{if } l \leq d \\ eGd & \text{if } l > d \end{cases} \tag{2.3}$$

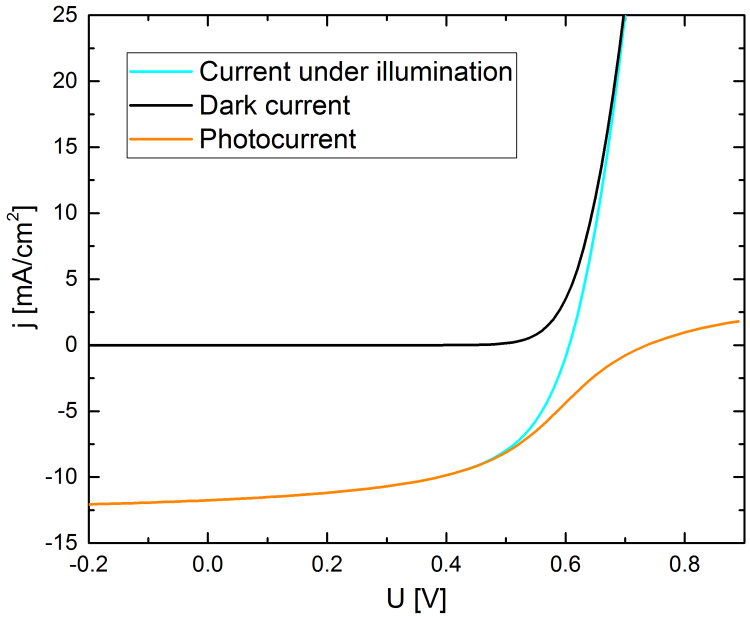

Figure 2.5: J-U curve showing the diode current J_{dark} and the current that arises from photogenerated charges J_{photo}. The total current under illumination is given by the sum of these, $J_{\text{illu}} = J_{\text{dark}} + J_{\text{photo}}$.

where G is the generation rate of free charges. The separate currents that make up the J-U curve of a solar cell under illumination are shown in Figure 2.5.

Two defining values for solar cells are the short circuit current J_{sc} and the open circuit voltage V_{oc}. At short circuit under illumination J_{sc} is obtained, this is the current of photogenerated charge extracted by the built-in potential. At open circuit, when the potential difference between the electrodes is equal to V_{oc}, no net current flows through the device and instead all photogenerated charges decay through recombination. The maximum power output P_{max} of a solar cell is given by the maximum value of the product $J \cdot U$, given by $J_{\text{max}} V_{\text{max}}$. P_{max} can also be expressed in terms of J_{sc} and V_{oc}, as well as the fill factor FF. The fill factor is defined as the ratio between the maximum power output P_{max} and the product $J_{sc} V_{oc}$, illustrated in Figure 2.6. Rearranging the terms the following expression is obtained for P_{max}:

$$P_{\text{max}} = J_{\text{max}} V_{\text{max}} = FF J_{sc} V_{oc}. \tag{2.4}$$

This way material dependent loss mechanisms, such as recombination, can be attributed mainly to FF, while V_{oc} and J_{sc} depend more strongly on device properties, such as the band gap. To obtain the efficiency η of the solar cell the maximum power output is simply divided by that of the incident photon flux P_{flux}:

$$\eta = \frac{P_{\text{max}}}{P_{\text{flux}}} = \frac{FF J_{sc} V_{oc}}{P_{\text{flux}}}. \tag{2.5}$$

A better understanding of the impact of individual loss mechanisms would make it possible to design efficient solar cells without time-consuming trial and error. In practice, it is very difficult to change a single parameter without affecting the rest. Computer simulations come in handy as the individual properties can be changed and the performance tuned. However, constructing the model requires a good understanding of the phenomena occurring in the device.

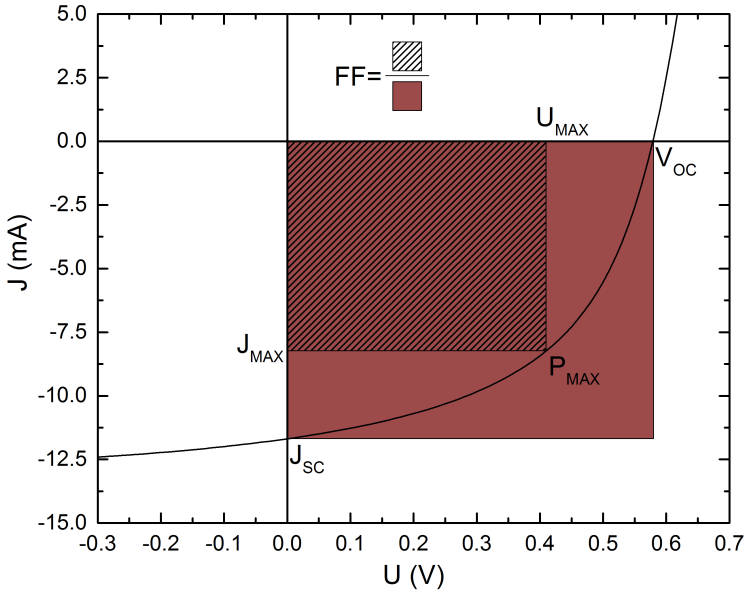

Figure 2.6: J-U curve showing the maximum power output $P_{\max}$ and its components. The fill factor is given by the area marked with black lines divided by the red rectangle, as shown in the figure.

2.2.2 Organic Materials as Photovoltaics

Organic materials have a very high absorption coefficient allowing for active layer thicknesses on the order of 100 nm [7]. Organic materials also generally have a wide absorption spectrum, thus making it possible to absorb a relatively large part of the incoming photon flux. The first organic photovoltaic devices, using tetracene among others as semiconducting layer, showed poor efficiencies of below 0.05% [8]. A major breakthrough was achieved when an efficiency of 1% was demonstrated by utilizing an active layer consisting of a donor and acceptor in a bi-layer structure [9].

In a bulk heterojunction solar cell the donor and acceptor materials are blended, thus increasing the probability that photogenerated excitons reach an interface before decaying. The finger structure shown in Figure 2.7 has been proposed as the ideal morphology for the active layer of a bulk heterojunction solar cell [10]. In this structure, charges can be transported to the desired electrodes without obstructions. As the pure phases are exclusively in contact with the appropriate electrode, no charges diffuse to the wrong electrode. Additionally, the spacing between the phases is small enough that most charges are dissociated while minimizing recombination. In reality, the active layer takes on a structure of randomly intertwining phases with isolated lumps that will not contribute to charge transport at all. The morphology of real devices can be studied with an atomic force microscope and one such image is shown in Figure 2.8 [11].

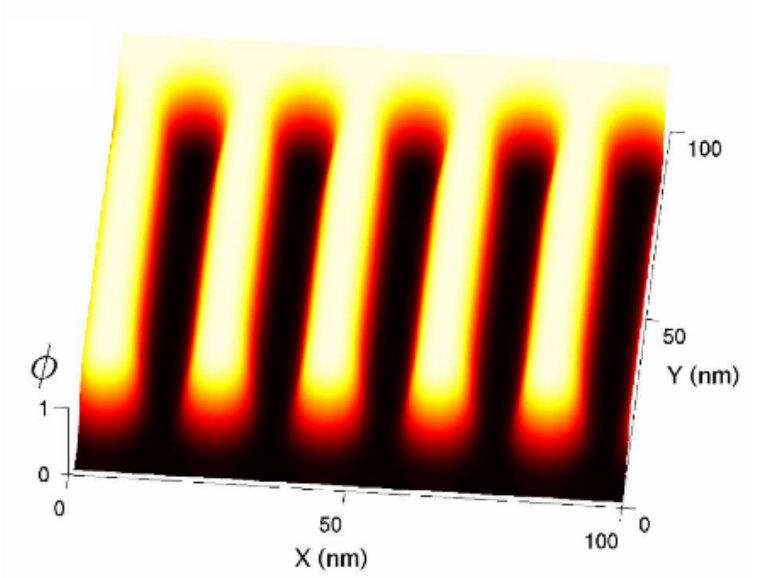

Figure 2.7: Morphology of a bulk heterojunction solar cell under optimal conditions, calculated by G. Buxton and N. Clarke [10]. The donor is given by the lighter color, $\phi = 1$ and the acceptor by the darker regions, $\phi = 0$.

Figure 2.8: Modified cross-section image of rrP3HT:PCBM (white:black) obtained with AFM by J Moon *et al* [11]. The bulk heterojunction structure show columnlike phases with mean pathway width of 12 nm.

Chapter 3

Theory on Charge Transport in Semiconductors

A more detailed description of charge transport in a semiconductor will now be presented. The reader is encouraged to consider how the various assumptions and simplifications relate to the theory of organic semiconductors presented in the previous chapter.

3.1 Energy Levels

3.1.1 Electrochemical Potential

The electrochemical potential η is the sum of electric and chemical potential, ψ and ξ respectively.

$$\eta_n = \xi_n - e\psi. \tag{3.1}$$

At thermodynamic equilibrium the electrochemical potential is also called the Fermi level E_F. The vacuum level E_{vac} is defined as the energy of an electron at rest in vacuum. This energy is not a constant and may have local variations due to charge imbalances. The zero energy level ($E = 0$) in this work will be defined as the vacuum level at a large distance from the material to avoid surface effects. The zero energy level is then independent of material properties and local potential shifts.

The work done when moving an electron from the conduction band to the (local) vacuum level is known as the electron affinity (EA). Similarly, the energy required to move an electron from the valence band to the vacuum level is called the ionization energy (IE). The chemical potential for electrons ξ_n and holes ξ_p is the sum of the material-dependent part EA, IE and a part dependent on carrier concentrations $\zeta_n(n), \zeta_p(p)$.

$$\begin{aligned} \xi_n &= EA + \zeta_n(n) \\ \xi_p &= IE - \zeta_p(p). \end{aligned} \tag{3.2}$$

At thermodynamic equilibrium the chemical potentials for electrons and holes are equal and given by

$$\xi_n = \xi_p = E_F - E_{vac}. \tag{3.3}$$

The components of the electrochemical potential at thermodynamic equilibrium are illustrated in Figure 3.1.

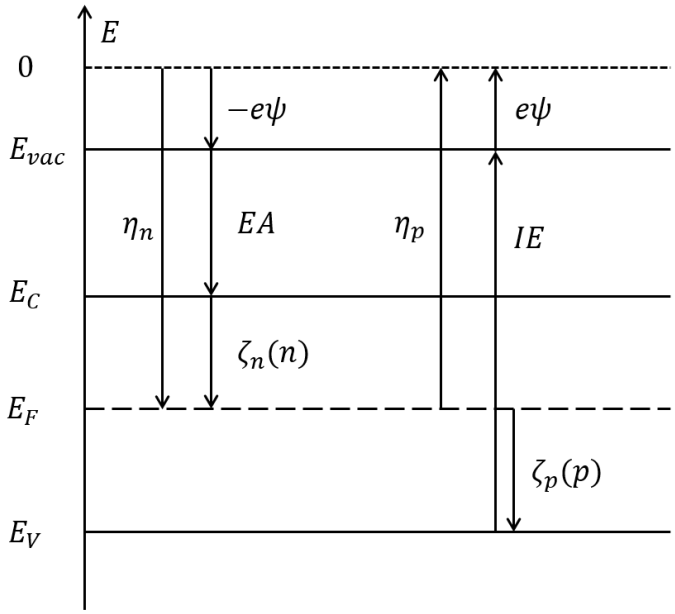

Figure 3.1: Energy diagram showing the components of the electrochemical potential for electrons and holes $\eta_{n,p}$. The chemical potential $\xi_{n,p}$ is divided into a constant, material dependent component EA, IE and a component determined by the concentration of free charges $\zeta_n(n), \zeta_p(p)$. The sum of electric ψ and chemical ξ potential determines the electrochemical potential.

3.1.2 Fermi Statistics

The energetic distribution of charge carriers in a material in thermodynamic equilibrium is described by the Fermi-Dirac distribution function. If the temperature T and Fermi level E_F are known, the probability of finding one electron at a state with energy E is given by:

$$f(E) = \frac{1}{\exp\left(\frac{E-E_F}{kT}\right)+1}. \tag{3.4}$$

For metals the Fermi level is located in the conduction band, giving rise to the high concentration of conduction electrons. In semiconductors the Fermi level is found in the middle of the band gap $E_g = E_V - E_C$ where no states are available. Since $E_g >> kT$ in a semiconductor, almost no electrons are found in the conduction band at thermodynamic equilibrium.

In a single level model the conduction band is assumed to have an energy E_C and an effective density of states N_C, which is the concentration of available states in the band. Similarly, holes are transported in the valence band with energy E_V and effective density of states N_V. This way the electron concentration in the conduction band n is simply given by

$$n = N_C \frac{1}{\exp\left(\frac{E_C-E_F}{kT}\right)+1} \tag{3.5}$$

at thermodynamic equilibrium. For energy differences $E_C - E_F$ that are large compared to kT the Boltzmann approximation can be used:

$$n = N_C \exp\left(\frac{E_F - E_C}{kT}\right). \tag{3.6}$$

The concentration of holes p in the valence band can be found in a similar manner,

$$p = N_V \exp\left(\frac{E_V - E_F}{kT}\right). \tag{3.7}$$

For small electron concentrations in the conduction band, this model describes the bottom of the band well but otherwise the width of the DOS should be considered. In a similar manner, the model also describes small concentrations of holes at the top of the valence band well. At thermodynamic equilibrium, an intrinsic semiconductor will have an equal amount of thermally excited electrons and holes. The concentration depends only on the band gap E_G and is called the intrinsic density n_i^2

$$np = n_i^2 = N_C N_V \exp\left(-\frac{E_G}{kT}\right). \tag{3.8}$$

The thermally generated charges still need to be separated into free charge carriers and, therefore, intrinsic carriers are generated at acceptor-donor interfaces.

A common Fermi level for electrons and holes is observed in pristine semiconductors at thermodynamic equilibrium, but is no longer true if free carriers are added to the system. If the relaxation within the bands happens on a short time scale compared to that between bands, an internal thermal quasi-equilibrium is reached separately for both types of charge carriers. Separate quasi-Fermi levels $E_F^{n,p}$ then describe the concentration of electrons in the conduction band and holes in the valence band. The quasi-Fermi levels are equal to the electrochemical potentials of the respective carrier type:

$$\begin{aligned} E_F^n &= \eta_n \\ E_F^p &= \eta_p. \end{aligned} \tag{3.9}$$

When free electrons are added to the semiconductor, the quasi-Fermi level for electrons is displaced towards the conduction band and now properly describes the electron concentration in the band. The quasi-Fermi level for electrons E_F^n is shown in Figure 3.2, similarly a separate quasi-Fermi level for holes is formed closer to the valence band if free holes are added.

Fermi-statistics can still be used in order to describe the concentrations of free charge carriers. The distribution then describes the electron concentration in the conduction band and hole concentration in the valence band separately. Using the separate quasi-Fermi levels, the charge carrier concentrations are given by

$$\begin{aligned} n &= N_C \exp\left(\frac{E_F^n - E_C}{kT}\right) \\ p &= N_V \exp\left(\frac{E_V - E_F^p}{kT}\right). \end{aligned} \tag{3.10}$$

Since additional charge carriers have been added to the system, the product np is no longer equal to the intrinsic carrier density and an additional factor now appears:

$$np = N_C N_V \exp\left(-\frac{E_G}{kT}\right) \exp\left(\frac{E_F^n - E_F^p}{kT}\right). \tag{3.11}$$

In a solar cell free charge carriers are mainly added by photogeneration. Photogenerated charges typically relax within their respective band on a much shorter time scale than that on which inter-band relaxation (recombination) occurs. Determining the quasi-Fermi levels, however, is generally not straightforward.

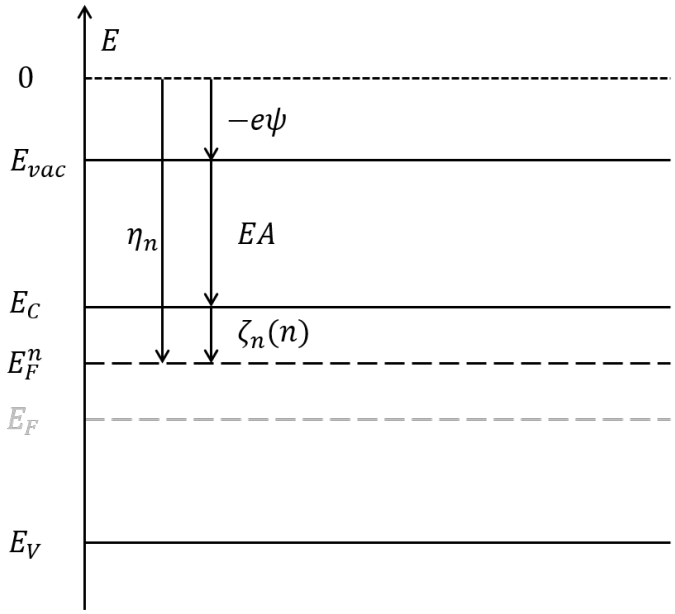

Figure 3.2: Energy diagram showing the components of the quasi-Fermi level for electrons. The change in the chemical potential determines the shift of the new quasi-Fermi level from the equilibrium position.

3.2 Charge Transport

In a solar cell the chemical energy of electron-hole pairs is converted into an electrical current. The driving forces giving rise to the current in a solar cell are the electric field $\bar{F}$ and the concentration gradients ∇n and ∇p. It is generally assumed that temperature gradients, gravitation and magnetism do not affect the current in any significant way.

3.2.1 Drift

The drift current describes movement of charged particles, in this case electrons and holes, in the presence of an electric field. The drift velocity $\bar{v}_{\text{drift}}$ of an electron is given by

$$\bar{v}_{\text{drift}} = -\mu\bar{F} \tag{3.12}$$

where μ is the mobility. The mobility describes how well an electron or hole can move through the material. The temperature and field dependence of the mobility was discussed briefly in Chapter 2.1.3. Differences between the mobility of electrons and holes in a single material are also often observed. The mechanisms causing the asymmetry are material-dependent and will not be discussed in detail. Now the total drift current can be calculated by considering the number of charged particles moving with drift velocity

$$\bar{j}_{\text{drift}} = -en\bar{v}_e + ep\bar{v}_p = e\bar{F}(n\mu_n + p\mu_p). \tag{3.13}$$

The electric field can be expressed in terms of electric potential, as $\nabla\psi = \bar{F}$, relating back to the previously discussed energy diagram. The drift current is then given by

$$\bar{j}_{\text{drift}} = -e\nabla\psi\ (n\mu_n + p\mu_p), \tag{3.14}$$

in this form the relation between the electric potential and the current is seen more clearly.

3.2.2 Diffusion

A diffusion current arises when a gradient in the charge carrier concentration is found in a system. Fick's law gives a relation between the electron diffusion current $\bar{j}^n_{\text{diff}}$ and ∇n:

$$\bar{j}^n_{\text{diff}} = eD_n \nabla n \tag{3.15}$$

where D_n is the diffusion coefficient for electrons. A relation between the diffusion coefficient and the mobility is given by the Einstein relation,

$$D_{n,p} = \mu_{n,p} \frac{kT}{e}. \tag{3.16}$$

The total diffusion current is obtained when including diffusion of holes. Note the opposite sign as the chemical potential is balanced by moving carriers away from positions where the concentration is larger than that of the surrounding, independent of charge

$$\bar{j}_{\text{diff}} = e(D_n \nabla n - D_p \nabla p) = kT(\mu_n \nabla n - \mu_p \nabla p). \tag{3.17}$$

The concentration gradients can also be expressed in terms of chemical potential by using Equation 3.6 and 3.2:

$$\nabla n = \frac{n}{kT} \nabla \xi_n. \tag{3.18}$$

Similarly to the drift current, the diffusion current can be described by the chemical potential

$$\bar{j}_{\text{diff}} = n\mu_n \nabla \xi_n - p\mu_p \nabla \xi_p. \tag{3.19}$$

3.2.3 Total Current

The total current for electrons and holes is given by the sum of the drift and diffusion currents. By writing the drift and diffusion current as functions of the electric and chemical potential, the net current can be described by the quasi-Fermi levels

$$\begin{aligned} \bar{j}_n &= e\bar{F} n\mu_n + eD_n \nabla n = -en\mu_n \nabla \psi + n\mu_n \nabla \xi_n = n\mu_n \nabla E_F^n \\ \bar{j}_p &= e\bar{F} p\mu_p - eD_p \nabla p = -ep\mu_p \nabla \psi - p\mu_p \nabla \xi_p = p\mu_p \nabla E_F^p. \end{aligned} \tag{3.20}$$

Note that the drift and diffusion current may be of either equal or opposite sign. This confusion is avoided by considering the gradient of the quasi-Fermi levels as the driving force.

3.3 Recombination Processes

Recombination is one of the main loss mechanisms in solar cells, describing the annihilation of electrons and holes. Recombination may occur when two charge carriers of opposite charge meet in space. The recombination rate R gives the rate

at which free charge carriers are lost to recombination. It is included in the continuity equation when written separately for electrons and holes,

$$\begin{aligned} \frac{\partial n}{\partial t} - \frac{1}{e}\nabla \cdot \bar{J}_n &= -R \\ \frac{\partial p}{\partial t} + \frac{1}{e}\nabla \cdot \bar{J}_p &= -R. \end{aligned} \tag{3.21}$$

In addition to recombination of free charge carriers, excitons and trapped charges may be involved in recombination processes. The most important recombination processes in organic solar cells are the bimolecular and the trap-assisted recombination. The rate of recombination via other mechanisms such as Auger recombination, describing recombination of three charges that meet in space, are small in comparison.

3.3.1 Bimolecular Recombination

Bimolecular recombination describes the rate of recombination of two free charges. The bimolecular recombination rate is proportional to the product of the carrier concentrations,

$$R = \beta np \tag{3.22}$$

where β is called the bimolecular recombination coefficient. There are several proposed expressions for β, considering how quickly charge carriers can find each other and the probability of re-dissociation. One commonly used expression for β is given by the Langevin theory, which simply considers the probability that carriers will meet in space [12]. The Langevin recombination constant β_L is given by:

$$\beta_L = \frac{e}{\epsilon\epsilon_0}(\mu_n + \mu_p). \tag{3.23}$$

The Langevin theory was developed for pristine materials and it has been shown to give inaccurate recombination rates in organic solar cells [13, 14]. It is still often used as a baseline, since it is the expected recombination rate in low-mobility materials.

3.3.2 Trap-Assisted Recombination

Trap-assisted recombination describes how one trapped and one free charge carrier recombine. Deep trap states will capture charge carriers, which will remain trapped for a significant amount of time before they are released or recombine with free charge carriers. An expression for the recombination rate can be derived by considering the Coulomb attraction between trapped charges and free charges of opposite sign. This was done by W. Shockley and W. Read [15] and the following expression was found,

$$R_{SRH} = N_t C_n C_p \frac{np}{C_n(n + n_{\text{thermal}}) + C_p(p + p_{\text{thermal}})}. \tag{3.24}$$

Here N_t is the trap density and $n_{\text{thermal}}, p_{\text{thermal}}$ are the concentrations of electrons and holes, which have been thermally excited from the conduction and valence band. These can be calculated according to:

$$\begin{aligned} n_{\text{thermal}} &= N_c \exp\left(\frac{E_t - E_c}{kT}\right) \\ p_{\text{thermal}} &= N_v \exp\left(\frac{E_v - E_t}{kT}\right) \end{aligned} \tag{3.25}$$

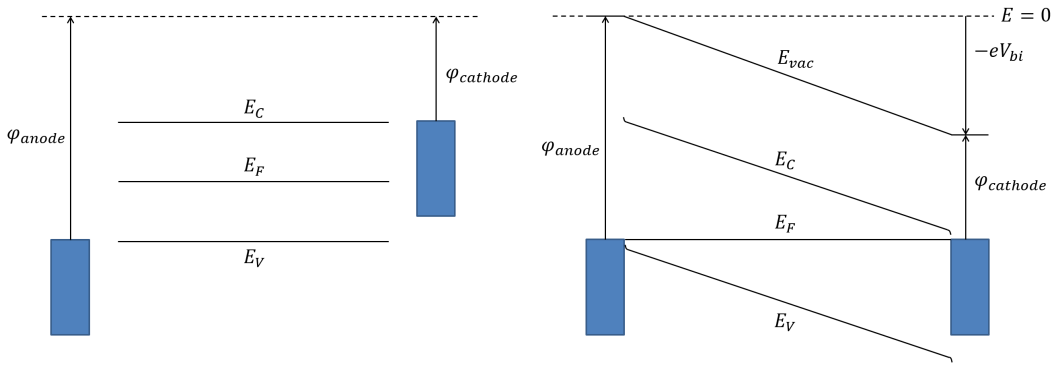

Figure 3.3: Energy diagram showing the electrode work functions, Fermi levels and transport level for electrons and holes E_C and E_V. The left diagram shows the energy levels of the individual materials before contact. The right diagram shows the energy levels of the system after contact at thermodynamic equilibrium.

where E_t is the energy level of the trap state. The capture coefficients $C_{n,p}$ are usually assumed to be given by expressions similar to those found in the Langevin theory,

$$C_{n,p} = \mu_{n,p}\frac{e}{\epsilon\epsilon_0}. \tag{3.26}$$

3.4 Solar Cell Operation

To be able to extract photogenerated charge carriers, an anode and a cathode must be connected to the semiconducting active layer. In the ideal case, ohmic contacts are formed between the electrodes and the active layer. An ohmic contact is able to extract and inject charge at a near infinite rate, meaning that the electrode is always in thermodynamic equilibrium with the semiconductor. When two electrodes with a difference in work functions $\Delta\varphi = \varphi_{\text{cathode}} - \varphi_{\text{anode}}$ are connected to the active layer an electric potential difference is formed over the layer. The difference in electric potential is called the built-in potential V_{bi}. When the system reaches thermodynamic equilibrium the Fermi level is constant throughout the device. The energy levels before and after connecting the electrodes are illustrated in Figure 3.3.

Under illumination free charge carriers are generated in the active layer and the system is no longer in thermodynamic equilibrium. The charge carriers can instead be described by separate quasi-Fermi levels. The Fermi level of the ohmic electrodes remains unchanged as long as no external bias is applied. The electrodes remain in thermodynamic equilibrium with the active layer at the interface, meaning that the quasi-Fermi levels are equal right next to the electrodes. At short circuit a current will flow through the device, described by the gradient of the quasi-Fermi levels. The potential difference between the electrodes is directly related to their Fermi levels, as well as that of the semiconductor at the electrode interface in the case of ohmic contacts,

$$V_{\text{anode}} - V_{\text{cathode}} = U = -(E_F^{\text{anode}} - E_F^{\text{cathode}})/e. \tag{3.27}$$

At open circuit no driving force excists, seen as constant quasi-Fermi levels throughout the active layer. As a result of this, no current flows through the device and all

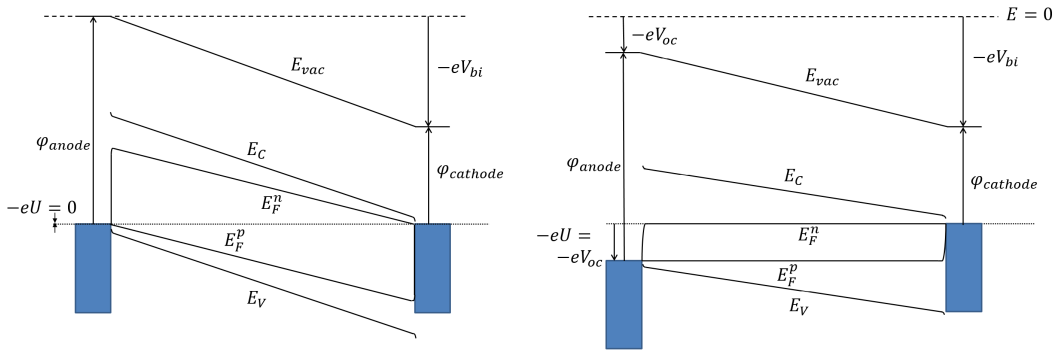

Figure 3.4: Schematic energy diagram at sort circuit J_{sc} (left) and open circuit V_{oc} (right). The potential difference between the electrodes U can be determined from the difference of the quasi-Fermi levels at the electrodes, as shown in the diagrams. At open circuit it can be seen that $U = V_{oc}$.

photogenerated charge carriers recombine. Fermi statistics (Equation 3.11) can be used to find an expression for V_{oc};

$$V_{oc} = \frac{1}{e}\left(E_g + kT \ln \frac{np}{N_C N_V}\right). \tag{3.28}$$

The energy diagrams for both J_{sc} and V_{oc} are shown in Figure 3.4.

In the absence of photogeneration and at low values for the potential U the current J_{dark} is simply that of a diode. The ideal diode current, often used for the dark current of solar cells, is given by [16]

$$J_{diode} = J_0 \left(\exp\left(\frac{eU}{kT}\right) - 1\right) \tag{3.29}$$

where J_0 is a constant, material dependent parameter. When the applied voltage is increased further, the space-charge limited regime is reached, meaning that the Coulomb potential of injected charges prevent additional injection. If both carrier types are injected and Langevin recombination is assumed, the space-charge limited current is given by

$$J_{\text{SCLC}} = \frac{9}{8}\epsilon\epsilon_0 \bar{\mu} \frac{U^2}{L^3}, \tag{3.30}$$

where L is the thickness of the active layer and $\bar{\mu} \approx \mu_n + \mu_p$ [17].

Chapter 4

Numerical Model

In order to solve a set of coupled equations that describe the transport of electrons and holes, a numerical model has been created. The assumptions and approximations required in order to obtain a numerical solution are described in this chapter. The specific model of the interface used to obtain the simulation results discussed in Chapter 5 is also presented.

4.1 The Charge Transport Problem

The movement of charges is described by drift and diffusion currents, but these equations do not contain information about the electric potential or the positions of the charges. The relation between charge carrier concentrations and electric potential is given by the Poisson equation

$$\nabla^2\psi = \frac{n - p + Q}{\epsilon\epsilon_0}. \tag{4.1}$$

The concentration of stationary charges such as dopants or trapped charges are described by Q. The concentration of charges occupying a trap state, n_t and p_t, when the system is in a steady state is given by [15]:

$$\begin{aligned} n_t &= N_{nt}\frac{C_n\ n + C_p\ p_{\text{thermal}}}{C_n(n + n_{\text{thermal}}) + C_p(p + p_{\text{thermal}})} \\ p_t &= N_{pt}\frac{C_p\ p + C_n\ n_{\text{thermal}}}{C_n(n + n_{\text{thermal}}) + C_p(p + p_{\text{thermal}})} \end{aligned} \tag{4.2}$$

where $N_{nt,pt}$ are the concentrations of electron and hole traps. The expressions for n, p_{thermal} and $C_{n,p}$ are given in equations 3.25 and 3.26.

The continuity equations describe the rate of change of free electrons and holes, thus relating the generation and recombination to the transport of charges. The continuity equations are given by the following expressions:

$$\begin{aligned} \frac{\partial n}{\partial t} &= \frac{1}{e}\nabla\cdot\bar{J}_n + G - R \\ \frac{\partial p}{\partial t} &= -\frac{1}{e}\nabla\cdot\bar{J}_p + G - R. \end{aligned} \tag{4.3}$$

The recombination rate used for R is the sum of the Langevin and SRH recombination rates given in equation 3.22 and 3.24. A constant generation rate G has been

assumed for the parts of the active layer where generation occurs. In reality the light intensity and consequently the generation decreases as the light travels through the active layer of the solar cell. The hole and electron currents describe the transport of the charge carriers and are given by equation 3.20. Note the time derivatives are equal to zero at steady state.

The system of equations consisting of Poissons equation and the continuity equations can be solved in order to obtain the free charge carrier concentrations, the potential and the current density as a function of position. In the transient case, a time and position dependent solution is found. The quasi-Fermi levels can be calculated when the electric potential and charge carrier concentrations are known, thus relating back to the electrochemical potential.

4.2 Numerical Methods

4.2.1 Normalization

The values of quantities involved in the calculations vary over different magnitudes and the equations contain a number of physical constants. The computation time of any calculation increases with the number of mathematical operations and is significantly more time-consuming when working with numbers that are not of the order of unity. It is therefore very important to properly normalize all quantities from a programming perspective. The normalization parameters used are presented in Table 4.1 and can be obtained by matching units of the physical constants with those of the quantities. A detailed analysis on optimal normalization is found in *Analysis and Simulation of Semiconductor Devices* [18].

Physical Quantity	Normalization Factor
ψ	$V_0 = \frac{kT}{q}$
x, y	$L = 100\ \text{nm}$
$\mu_{n,p}$	$\mu_0 = 10^{-7}\frac{\text{m}^2}{\text{Vs}}$
n, p	$n_0 = \frac{V_0 \varepsilon \varepsilon_0}{qL^2}$
j	$j_0 = \frac{qV_0 n_0 \mu_0}{L}$
R, G	$R_0 = \frac{j_0}{qL}$

Table 4.1: Normalization parameters. The normalized quantity is obtained when dividing the original quantity with the normalization factor. The normalized potential ψ' is given by $\psi' = \psi / V_0$.

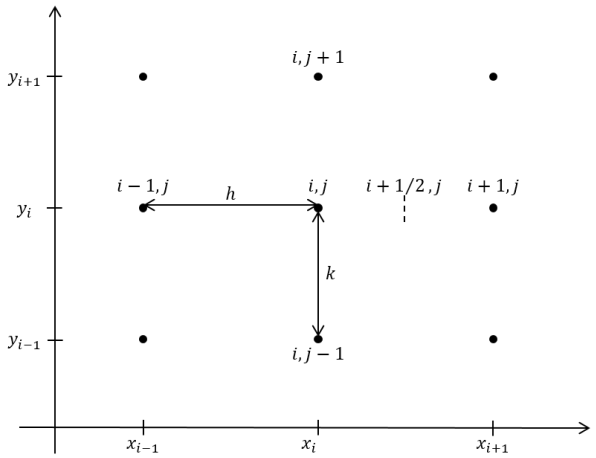

Figure 4.1: The active layer is divided into a lattice consisting of a number of points. Properties such as charge carrier concentrations are calculated for each point. Properties that depend on two adjacent points, such as the current or electric field, are calculated halfway between the points. All properties can be interpolated to any position in the active layer if necessary.

4.2.2 Discretization

To be able to solve the system of differential equations numerically, they need to be converted into difference equations. The difference equations can then be solved for each of a discrete set of positions and times. The first step is to divide the lattice into a number of discrete points N. For simplicity, the distances between points in x- and y-direction are assumed to be constant. The distance between two adjacent points in x-direction $x_{i-1,j}$ and $x_{i,j}$ is given by h and in the y-direction for $x_{i,j-1}$ and $x_{i,j}$ by k. In the case of a transient measurement, the time derivatives in the continuity equations need to be evaluated. The time coordinate is then discretized and the time difference between two points t_m and t_{m+1} is given by Δt. The notation used will be defined in the following way, for a function f:

$$f_{i,j,m} = f(x_i, y_j, t_m) \tag{4.4}$$

$$f_{i+1/2,j,m} = f(x_i + \frac{h}{2}, y_j, t_m) = f(\frac{x_i + x_{i+1}}{2}, y_j, t_m). \tag{4.5}$$

A schematic picture of the discretization of the lattice is seen in Figure 4.1.

Derivatives of first and second order of the potential can be approximated in the following way:

$$\frac{\partial \psi}{\partial x}\Big|_{i,j} = \frac{\psi_{i+1/2,j} - \psi_{i-1/2,j}}{h} \tag{4.6}$$

$$\frac{\partial^2 \psi}{\partial x^2}\Big|_{i,j} = \frac{\psi_{i+1,j} - 2\psi_{i,j} + \psi_{i-1,j}}{h^2}. \tag{4.7}$$

The same approximations can also be utilized when evaluating derivatives of the current densities, found in the continuity equations (Equation 4.3). The charge carrier concentrations n, p will generally have an exponential dependence on distance and special care has to be taken. The following discrete expressions for the derivatives of charge carrier concentrations were proposed by Scharfetter and Gummel [19]:

$$\frac{\partial n}{\partial x}\Big|_{i+1/2,j} = \frac{\psi_{i+i,j} - \psi_{i,j}}{\exp(\frac{\psi_{i+1,j} - \psi_{i,j}}{2}) - \exp(\frac{\psi_{i,j} - \psi_{i+1,j}}{2})} \cdot \frac{n_{i+1,j} - n_{i,j}}{h}. \tag{4.8}$$

Now the discrete versions of the continuity and Poisson equations can be obtained for the steady state. The electric field and the time derivatives can be approximated in the following way, provided that h, k and Δt are sufficiently small

$$F_{i+1/2,j} = -\frac{\psi_{i+1,j} - \psi_{i,j}}{h} \tag{4.9}$$

$$\frac{\partial n}{\partial t}|_{i,j,m+1} = \frac{n_{i,j,m+1} - n_{i,j,m}}{\Delta t}. \tag{4.10}$$

The charge carrier concentrations and potential at a point x_i, y_j can be calculated by solving the discrete continuity equation for holes and electrons and the Poisson equation at that point. When a solution is to be obtained for each of the N points of the active layer, a system of $3N$ equations needs to be solved. The expressions for the discrete equations are found in Appendix A.

4.2.3 Iterative Scheme

The successive over-relaxation (SOR) method is the iterative method that has been used to solve the system of $3N$ equations. The method is an extension of the Gauss-Seidel method with improved rate of convergence [20]. The system of equations can be written as a matrix equation of the form

$$\bar{\bar{A}}\bar{x} = \bar{b}, \tag{4.11}$$

where $\bar{x}$ contains the unknown variables. The matrix $\bar{\bar{A}}$ can then be decomposed into a diagonal matrix $\bar{\bar{D}}$ as well as a lower and upper triangular matrix $\bar{\bar{L}}$ and $\bar{\bar{U}}$. The equation system can then be rewritten in the following way:

$$(\bar{\bar{D}} + \omega\bar{\bar{L}})\bar{x} = \omega\bar{b} - (\omega\bar{\bar{U}} + (\omega - 1)\bar{\bar{D}})\bar{x} \tag{4.12}$$

where the constant ω is called the relaxation factor. The iteration scheme can now be obtained,

$$\bar{x}^{k+1} = (\bar{\bar{D}} + \omega\bar{\bar{L}})^{-1}(\omega\bar{b} - (\omega\bar{\bar{U}} + (\omega - 1)\bar{\bar{D}})\bar{x}^k). \tag{4.13}$$

The value for x_u^{k+1} can be expressed in terms of matrix elements a_{uv} of $\bar{\bar{A}}$:

$$x_u^{k+1} = (1 - \omega)x_u^k + \frac{\omega}{a_{uu}}(b_u - \sum_{v<u} a_{uv}x_v^{k+1} - \sum_{v>u} a_{uv}x_v^k), u = 1, 2, ..., N. \tag{4.14}$$

It is not straightforward to find the optimal value for ω, but under certain conditions it can be shown that the method always converges when $0 < \omega < 2$ [21]. In the simulations run in this work the value of ω has generally been in the range $1.6-1.95$.

4.3 Solution

The potential of the electrodes acts as boundary conditions for the system of equations in this model. An initial guess is required in order to initiate the iterative process. The potential generally has an approximately linear y-dependence, while the charge carrier concentrations decrease exponentially as a function of distance from the electrodes. These are examples of good initial guesses in a general case, but can be improved if the exact solution is familiar.

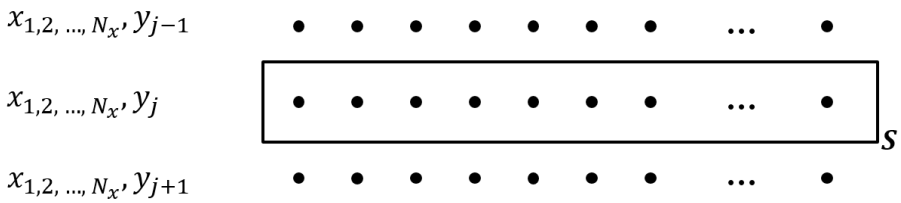

Figure 4.2: Schematic picture showing a surface S, surrounding the line of lattice points $x_{1,2,\ldots,N_x}, y_j$. The periodic boundary conditions ensure that the integral in Equation 4.16 is zero for the vertical sides of S. This can be pictured as an electron moving to the right at x_{N_x}, y_j and appearing, still moving in positive x-direction, to the left of x_1, y_j. As the surface integral is equal to zero, the current at $x_{1,2,\ldots,N_x}, y_{j-1/2}$ must equal to that at $x_{1,2,\ldots,N_x}, y_{j+1/2}$.

The approximate solution to the system of equations is reached when certain convergence criteria are satisfied. The criteria should be defined in such a way that a good solution is reached independently of what the solution is. A good example of this is to check if the change in a parameter is less than a certain fraction of the parameter value, in the case of the potential:

$$|\psi_{i,j}^{k+1} - \psi_{i,j}^{k}| < \delta \ |\psi_{i,j}^{k+1}| \tag{4.15}$$

where $\delta << 1$ determines how accurate the solution is.

By numerically solving the coupled differential equations, values for the potential and charge carrier concentrations are obtained for each lattice point. The current and electric field between each pair of adjacent points can then be calculated. The measured current density in an outer circuit is not directly obtained and therefore an analysis of the current density in the active layer has been done. The integral form of the continuity equation in steady state

$$\oiint_S \bar{j} \cdot d\bar{S} = 0 \tag{4.16}$$

is valid for any surface S, as long as no net charge is generated in the system. If the surface S is chosen to be a rectangular surface containing the points $(x_{1,2,\ldots,N_x}, y_j)$, where N_x is the total number of points in x-direction, the integral can be converted into a sum of the current at surrounding points. By choosing S so that it is located half-way between the chosen line of points and those next to it, as shown in Figure 4.2, the integral can be approximated by the sum

$$\sum_{j=1}^{N} \bar{j}_{i,j+\frac{1}{2}}^{y} - \bar{j}_{i,j-\frac{1}{2}}^{y}, \tag{4.17}$$

where $\bar{j}_{i,j}^{y}$ is the current in the y-direction. The periodic boundary conditions result in an equal current at $(x_{1/2}, y_j)$ and $(x_{N+1/2}, y_j)$ and thus the value of the integral at those sides is equal but of opposite sign. Remembering that the sum is equal to zero, it can be seen that the sum of the current for each row $(x_{1,2,\ldots N}, y_j)$ must be equal. The current density measured in an outer circuit $\bar{j}$ is given by the average

current density for a row,

$$\bar{j} = \frac{1}{N_x + 1} \sum_{i=0}^{N_x} \bar{j}_{i+1/2,j+1/2}. \tag{4.18}$$

In a one-dimensional model the same result is obtained directly from the differential form of the continuity equation,

$$\nabla \cdot \bar{j} = 0. \tag{4.19}$$

In that case the current is constant throughout the active layer and equal to that measured in the outer circuit. In the transient case, a more in-depth analysis is required.

4.4 Description of the Physical Properties of the Model

To reduce computation load and the complexity of the analysis of the data obtained from the simulation some approximations have been made. The main features of the model are presented below. The energy levels in this work have been chosen to those of P3HT:PCBM, which is one of the most studied bulk heterojunction systems.

4.4.1 The Interfacial Layer

To describe the interface between the acceptor and donor without looking at individual sites is difficult and some simplifications are needed. In this model an interfacial layer has been utilized in a similar manner as done by F. Stelz and U. Würfel [22]. The interfacial layer acts as an effective semiconductor with HOMO and LUMO levels equal to that of the donor HOMO level and acceptor LUMO level respectively. The energy levels used in the model are depicted in Figure 4.3. This layer can be seen as the region where the phases mix and excitons can be separated into free charge carriers. If the entire active layer is set to be interfacial layer the commonly used one-dimensional effective semiconductor model is obtained.

The energy barriers found at the contacts and interface are included as probabilities of thermal excitations over the barriers. According to Boltzmann statistics, the probability of thermal excitation P_{thermal} over an energy barrier E_b is given by

$$P_{\text{thermal}} = \exp\left(-\frac{E_b}{kT}\right). \tag{4.20}$$

The transport levels E_V and E_C will be assumed to be approximately equal to the relevant HOMO and LUMO levels in the model.

In this work we will mainly focus on the finger structure shown in Figure 4.4, but slight modifications will be done when necessary. The comparison with theoretical predictions will be done for a similar structure, where the pure phases and interfacial layer extend all the way from the anode to the cathode. This structure is also better when comparisons to the one-dimensional model are done, as no charge selectivity for the electrodes is included in that case.

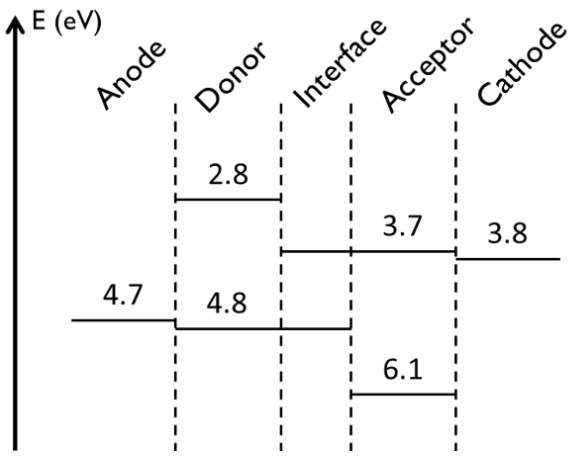

Figure 4.3: The energy levels of the electrodes, donor, acceptor and the interfacial layer. The interfacial layer acts as an effective semiconductor with the hole (electron) transport properties of the donor (acceptor).

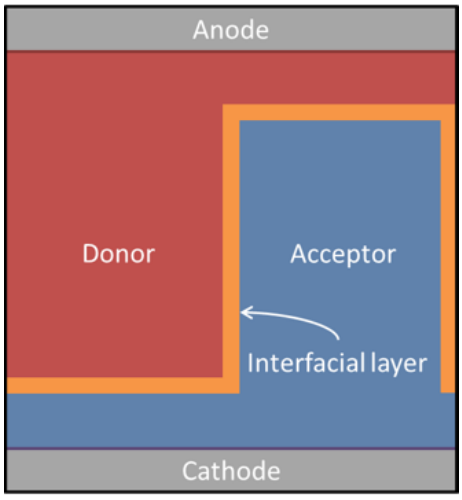

Figure 4.4: The finger structure of the morphology of the active layer mainly used in this work. The periodic boundary conditions create an infinite number of identical repeat-units. Under laboratory conditions the width of the solar cell is on the order of 1 mm, corresponding to 50 000 repeat units.

4.4.2 Generation and Recombination

Excitons in P3HT have a diffusion length of about 10 nm [23, 24], meaning that an exciton will diffusing 10 nm on average during its lifetime. As long as the distance to the nearest interface is smaller than the diffusion length most excitons should reach it and be separated before decaying. Assuming that the number of exciton-charge interaction events is small, the exciton problem is decoupled from that of the free charges and can be treated as a separate problem. In this model excitons are neglected and an effective generation of free charges at the interface is used instead.

Free charge carriers are generated at the interfacial layer, after which holes diffuse into the donor and electrons into the acceptor. The majority of recombination events between free charge carriers take place at the interface. Therefore, only trap states located in this region have a major impact on the total recombination. In this model the Langevin capture coefficients will be assumed for both bimolecular and trap-assisted recombination. The discretization of the recombination rates has been done by replacing n and p with $n_{i,j}$ and $p_{i,j}$ in Equation 3.22 and 3.24.

Chapter 5

Results

In this chapter, the viability of the model is discussed and the results are compared to theoretical predictions. A comparison to results obtained from a one-dimensional model is presented and an attempt to find effective parameters that replicate the results of the two-dimensional model is made when possible. The simulation parameters used are those presented in Table 5.1, unless specified otherwise.

Constant	Value
T	300 K
ε	3.4
L	100 nm
$d_{\text{interface}}$	1.5 nm
d_{phase}	8.5 nm
$\mu_{e,h}$	$1 \cdot 10^{-7}\text{m}^2\text{sV}^{-1}$
N_c, N_v	10^{-26}m^{-3}

Table 5.1: The value of parameters used in the simulation unless otherwise specified.

A number of different variations of the same basic finger structure for the active layer have been studied. The one-dimensional model does not prevent holes from reaching the cathode or holes from reaching the anode. For a better comparison the structure of the two-dimensional active layer can be modified, so that the pure phases reach both electrodes but are still separated by the interfacial layer, as seen

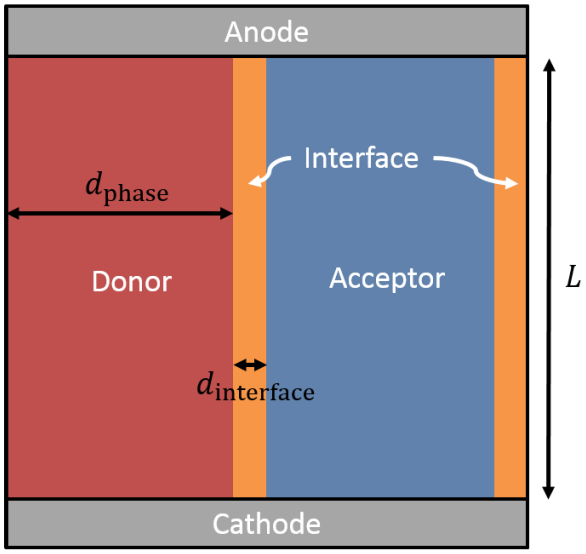

Figure 5.1: Modified active layer structure with non-selective contacts. Both charge carrier types can reach either electrode, thus making for a better comparison to the one-dimensional model. The values of the thicknesses are given in Table 5.1.

in Figure 5.1. In the case of interfacial trap states, a thicker interfacial layer is desirable in order to obtain the reported value of the dipole shift caused by trapped charges.

5.1 Basic Properties

An introduction to the charge transport properties will be given for the morphology shown in Figure 5.1, as the charge transport is fairly straightforward for this structure. The phases are separated by an interfacial layer and extend to both electrodes individually. At dark conditions all free charges in the active layer are either thermally generated at the interfacial layer or injected at the electrodes. The carrier concentrations at zero applied voltage are shown in Figure 5.2. When a potential is applied, the IV-curve is expected to follow the diode current expression given in Equation 3.29 and 3.30. A small current at negative bias arises from extraction of thermally generated charges. The dark current and theoretical expressions given in the aforementioned equations are illustrated in Figure 5.3.

Under illumination, a large amount of free charges are generated at the interfacial layer and the Fermi-level is split into quasi-Fermi levels. In addition to the diode current, the photocurrent is now also observable. Photogenerated electrons are transported to the cathode in the acceptor phase, as well as the interfacial layer. Correspondingly, photogenerated holes are transported to the anode in the donor phase and the interfacial layer. The separate components of the current at short circuit are shown in Figure 5.4. At open circuit conditions no current runs through the device, indicating that the quasi-Fermi levels or carrier concentrations are constant throughout the active layer. The charge carrier concentrations are seen to be equal and constant in the active layer excluding the regions close to the electrodes. The quasi-Fermi levels and carrier concentrations are shown in Figure 5.5 and 5.6.

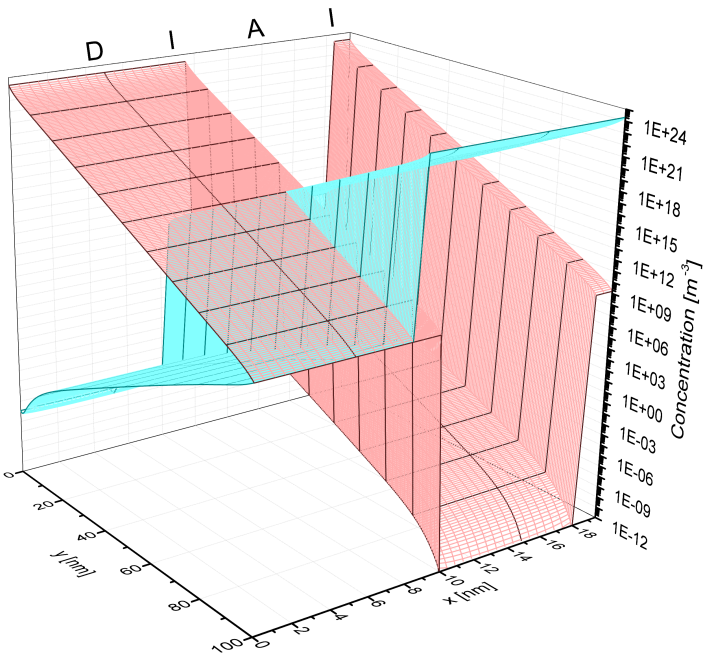

Figure 5.2: 3D plot of the hole- (red) and electron concentrations (blue) in the active layer at zero applied voltage and dark conditions. The donor, interface and acceptor are marked with "D", "I" and "A" for clarity. At thermodynamic equilibrium carriers diffuse far into the active layer.

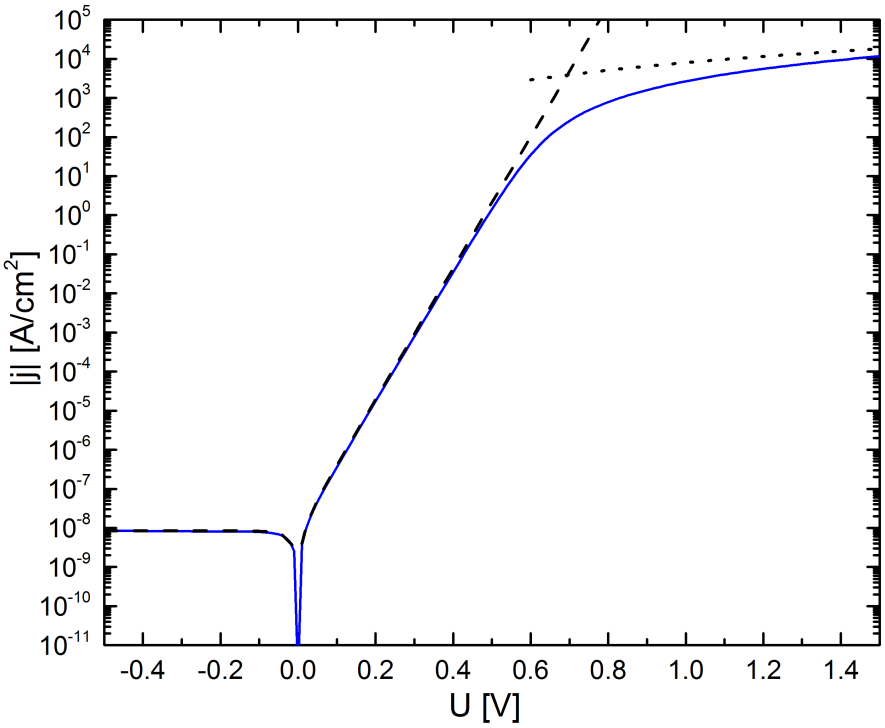

Figure 5.3: J-U curve showing the absolute value of the current at dark conditions. The dashed curve shows the ideal diode current given by equation 3.29. The dotted line represents the saturated space-charge limited current as per equation 3.30.

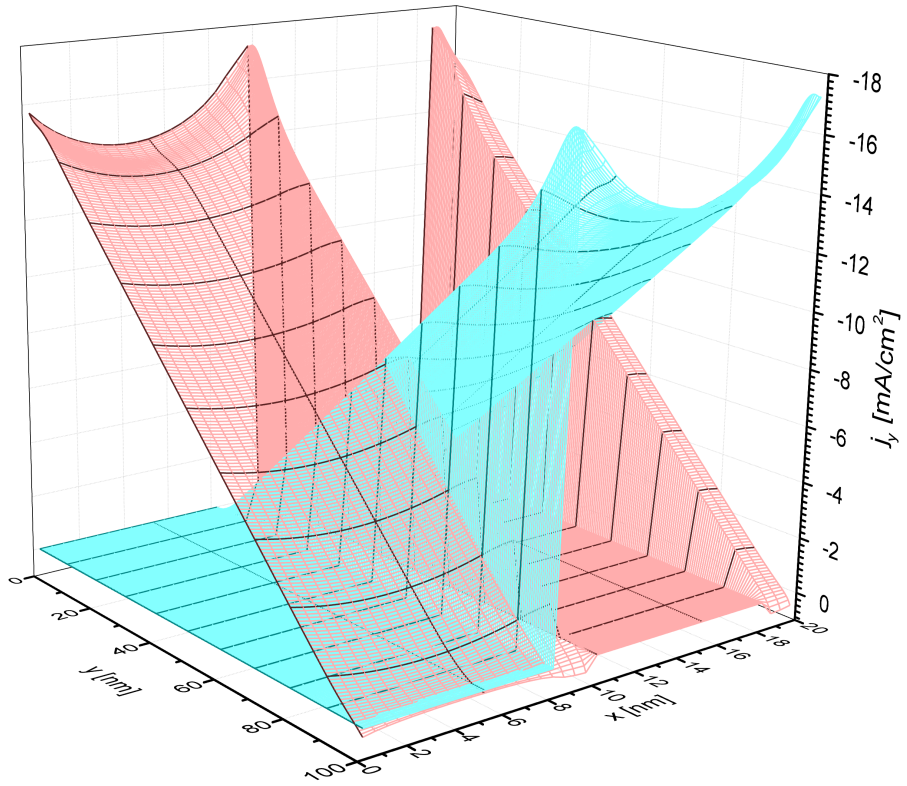

Figure 5.4: 3D plot of the y-component of the electron (blue) and hole current (red) at short circuit. The electron and hole currents are seen to occur in their respective phase, as well as at the interface. The measured current density in the outer circuit is the average of the y-component of the current densities.

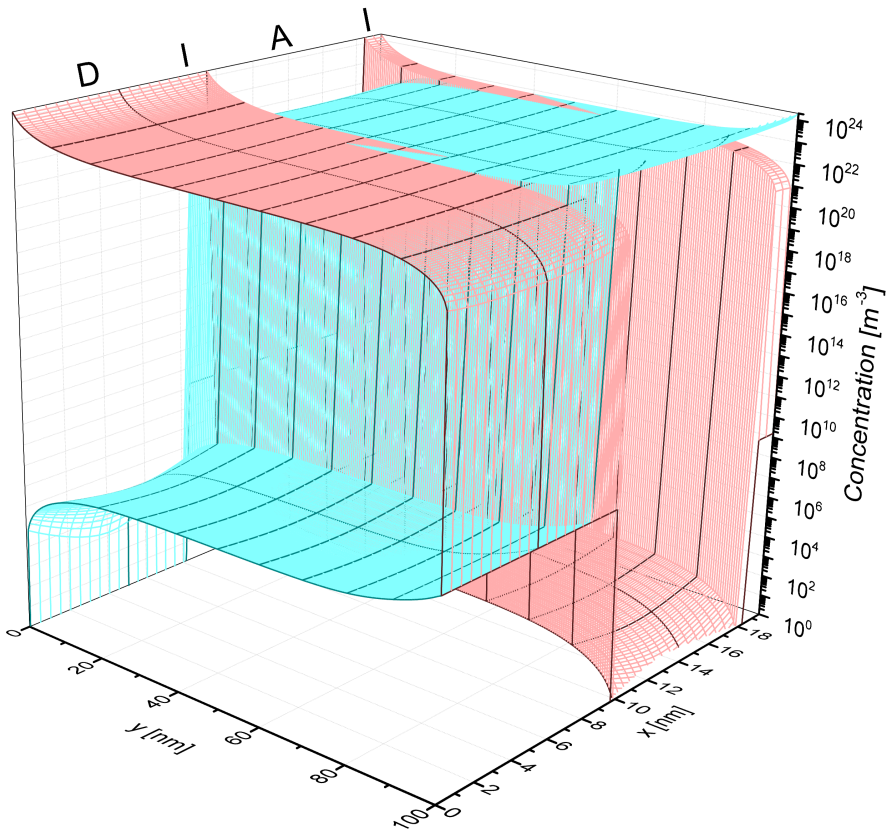

Figure 5.5: 3D plot of the hole (red) and electron concentrations (blue) in the active layer at open circuit. The hole (electron) concentration is high in the interfacial layer and the pure donor (acceptor) phase. The charge carrier concentrations are seen to be fairly constant and equal for both types in the center of the active layer.

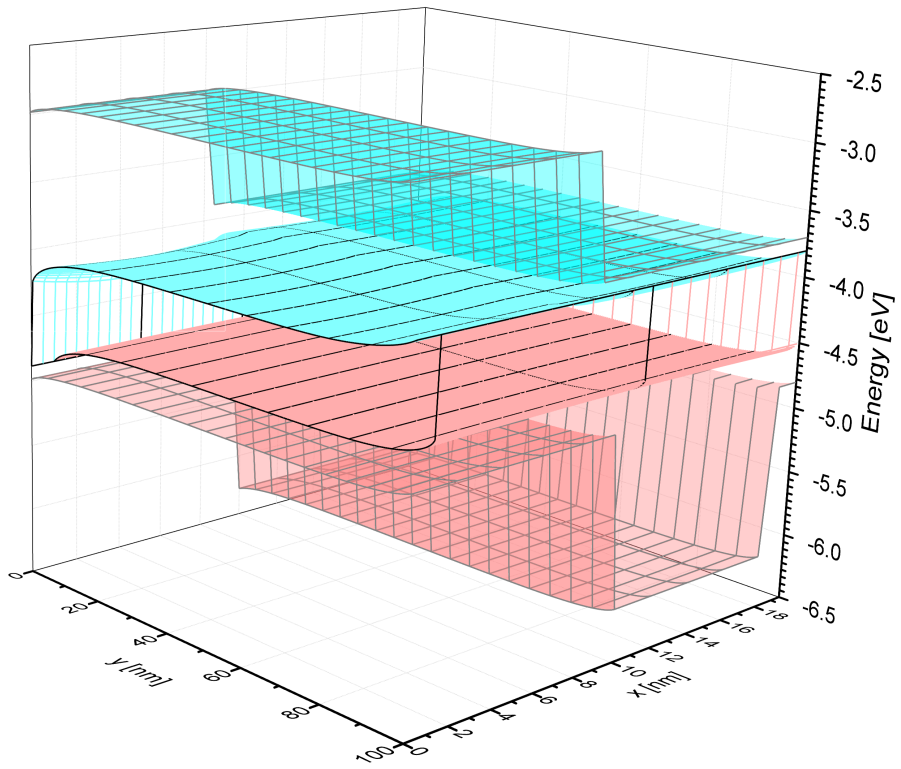

Figure 5.6: 3D plot of the quasi-Fermi levels for holes (red) and electrons (blue), as well as E_V (transparent red) and E_C (transparent blue) for each layer. The quasi-Fermi level for holes is close to E_V in the donor phase, describing the high concentration of holes seen in Figure 5.5, similarly for electrons. The quasi-Fermi levels are almost constant in the whole active layer, deviating slightly at the electrodes and the interface.

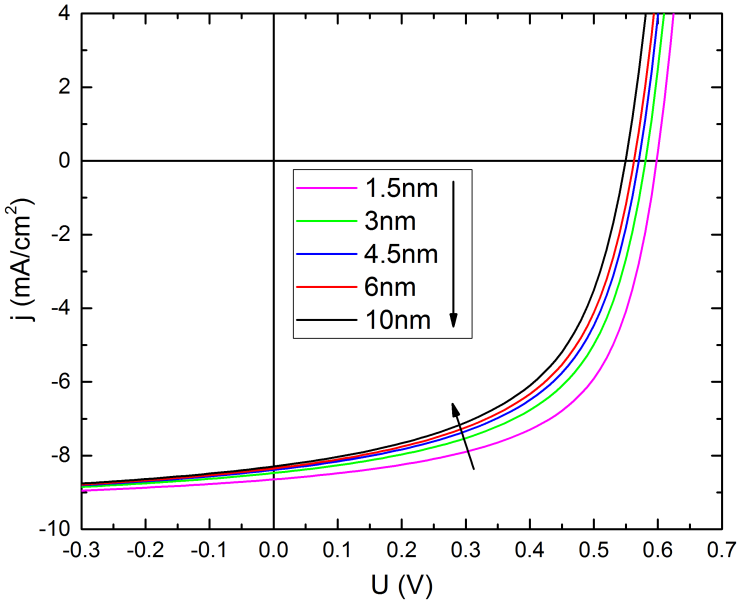

Figure 5.7: IV curves for different values of the interfacial layer thickness $d_{\text{interface}}$ with constant effective generation G_{eff}. When $d_{\text{interface}} = 10$ nm the interfacial layer covers the whole active layer, meaning that this is exactly equal to the one-dimensional case. A reduction in V_{oc} and J_{sc} is observed with increasing $d_{\text{interface}}$. Saturation to J_{photo} is almost reached at -0.3 V.

5.1.1 The Interfacial Layer

In a one-dimensional model, the effective semiconductor model used for the interface makes up the entire active layer. The differences between IV curves for a one- and two-dimensional model have been illustrated by increasing the width of the interfacial layer until the one-dimensional case is reached. For the results to be comparable, an equal amount of charge carriers have been generated in each case. This is done by keeping the effective generation rate G_{eff} constant for each case. The effective generation is a measure of the average free charge carrier generation in the active layer. If an equal amount of free charges are generated at each point of the active layer, $G = G_{\text{eff}}$. When generation of free charges only occurs at the interfacial layer the relation between G and G_{eff} is given by

$$G_{\text{eff}} = \frac{a_{\text{interface}}}{a_{\text{AL}}} G \tag{5.1}$$

where $a_{\text{interface}}$ and a_{AL} are the areas of the interfacial layer and the active layer, respectively. G_{eff} can also be determined from the photocurrent J_{photo}, at large negative values for U it is given by Equation 2.3,

$$J_{\text{photo}} = eG_{\text{eff}}d. \tag{5.2}$$

The current under illumination J_{illu} saturates at high negative applied voltage and is then equal to J_{photo}, since all photogenerated charge carriers are extracted. IV curves for varying interfacial layer thickness are shown in Figure 5.7.

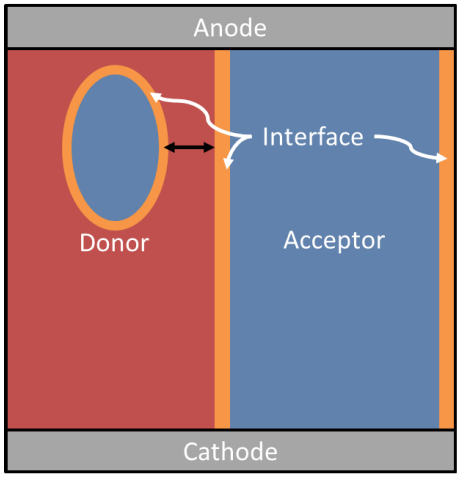

Figure 5.8: Modified active layer structure with an isolated domain of acceptor, inserted into the pure donor phase. The black arrow marks the distance between the isolated domain and the interfacial layer separating the pure phases. When this distance is larger than zero, the acceptor phase splits into the two domains seen in the figure.

5.1.2 Isolated Phase Lumps

In bulk heterojunction solar cells, isolated domains of either the donor or acceptor phase commonly occur, leading to an increased recombination rate. To study the effect of such domains the morphology seen in Figure 5.1 has been modified, as shown in Figure 5.8. For comparison with the case where the domain is completely isolated, it was moved so that it barely touches the interfacial layer to the right, connecting it to the rest of the acceptor. Holes are still free to move on both sides of the domain, as the pure acceptor phases are connected by the interfacial layer. In this way, the difference in transport properties for the two cases are minimized. In the case of the isolated domain, the amount of charge builds up in the domain until a steady state is reached, after which all electrons generated at the isolated domain recombine. Since all electrons generated at the isolated domain are lost to recombination, as well as an equal amount of holes, G_{eff} will remain the same even if no generation occurs at the lump.

If the transport efficiency is not significantly altered by the isolated domain, the IV curve should not change even if the isolated domain is removed completely, returning to the original structure shown in Figure 5.1. The two cases with an acceptor domain either connected to or isolated from the bulk of the acceptor are presented in Figure 5.9. A comparison to the original structure with the same value for G is also shown, representing a case where the excitons separated at the isolated domain are lost completely. As predicted, no significant change is seen when the isolated domain is removed completely.

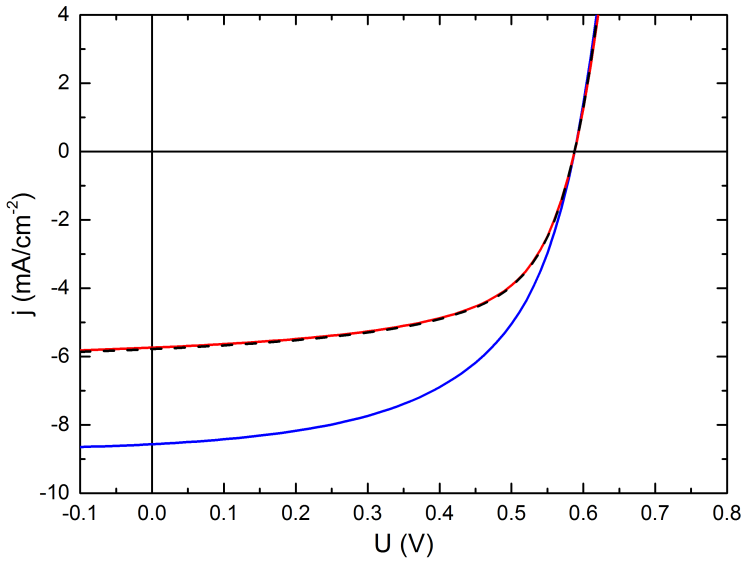

Figure 5.9: J-U curve for the structure shown in Figure 5.8. The blue curve shows the case where the domain is connected to the bulk of the acceptor. When the domain is isolated all charges generated there are lost and the red curve is obtained. The dashed black curve is obtained when the domain is removed completely but the amount of charges generated at the other interfaces is kept constant.

5.2 The Influence of Recombination

5.2.1 Langevin Recombination

To compensate for the lower recombination rate observed in experiments, a reduction factor γ is often included in the Langevin expression, given in Equation 3.22. Several explanations for the reduction factor have been presented. Among others, models taking into account the different time required for the two charges to reach the same interface [25] and the spatial variation [26] in the charge concentrations have been proposed. In the simulation, equal charge carrier mobilities have been used and the position dependence of the charge concentrations are taken into account.

In the two-dimensional model, charges are allowed to recombine anywhere but hole and electron concentrations are very small in the acceptor and donor, respectively, and in practice almost all recombination events take place at the interface. In contrast, in the one dimensional effective semiconductor model there are no areas of the active layer were only one charge carrier is present and as a result recombination occurs everywhere. In both cases, the recombination rate has been discretized so that only carrier concentrations at the specific point where the recombination event occurs are used,

$$R_{i,j} = \beta_{i,j} n_{i,j} p_{i,j}. \tag{5.3}$$

In Figure 5.10, the two dimensional case is compared to the one-dimensional effective semiconductor model with different values for the reduction factor γ. At open circuit conditions, the charge carrier concentrations of both carriers are mostly constant and equal throughout the interfacial layer as seen in Figure 5.5. The one dimensional solution is similar to that for the interfacial layer of the two dimensional case at open circuit, but the charge carrier concentrations are lower, $n, p \approx 10^{21}$ m^{-3}.

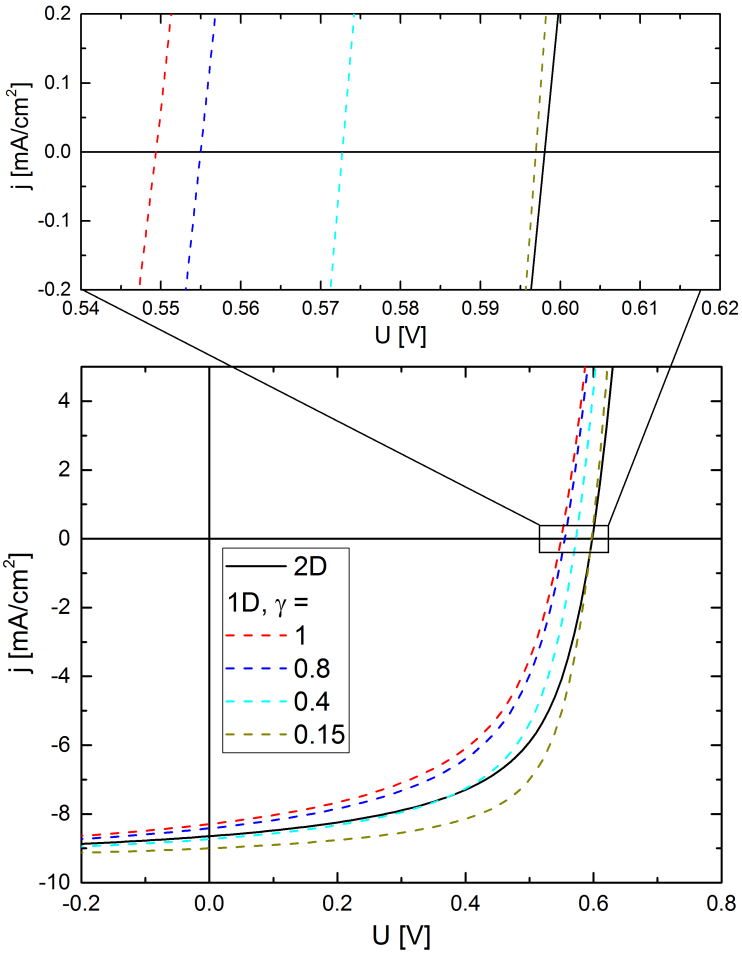

Figure 5.10: J-U curve showing the one-dimensional effective semiconductor model with various values for the recombination reduction factor γ (dashed curves), as well as the two-dimensional model (black curve). The Langevin expression has been used to describe recombination in both models, $R = \gamma\beta_L np$. In the two-dimensional model, $\gamma = 1$. The magnified part shows open circuit conditions for the curves.

Since no net current is allowed at open circuit, all charge carriers will effectively recombine at the exact position they are generated and the recombination rate is simply given by the rate of generation, $R = G$.

In Figure 5.10, the curves are seen to almost saturate to the same value at -0.2 V as a result of equal G_{eff} for the different cases. Since charges do not move at V_{oc}, the relevant generation rate in the two dimensional case is not G_{eff} but simply G. In the two-dimensional case, the area of the interfacial layer was 15% of the total active layer area, therefore $G_{\text{eff}}^{\text{2D}} = 0.15 \cdot G$ as given by Equation 5.1. Writing the equations for the two cases,

$$\begin{aligned} R^{\text{2D}} &= G^{\text{2D}} = \frac{G_{\text{eff}}}{0.15} \\ R^{\text{1D}} &= G^{\text{1D}} = G_{\text{eff}} \end{aligned} \tag{5.4}$$

where the subscripts 1D and 2D represent the one and two dimensional case, respectively. By solving for R^{1D}, a relation between the recombination rates is obtained

$$R^{\text{1D}} = 0.15 \cdot R^{\text{2D}}. \tag{5.5}$$

Thus, the recombination rate of the two-dimensional case effectively looks like reduced Langevin recombination with $\gamma = 0.15$ when compared to a one-dimensional model. This result should hold as long as the recombination is limited to a specific part of the active layer and generated charges remain mostly stationary after generation. These conditions will, however, most likely not be satisfied in real devices.

5.2.2 Interfacial Trap States

Integer charge transfer (ICT) states are described by the ICT-model [27] in systems where it is energetically favorable to transfer an electron from the donor to the acceptor. The model predicts that in some systems, electrons will spontaneously be transferred from the donor to the acceptor, leaving behind a hole. The two charges remain immobile after the transfer has occurred and the Coulomb interactions between the charges give rise to a dipole shift Δ. The dipole shift in the energy levels at the interface are predicted to be on the order of 0.3 eV for P3HT:PCBM [28].

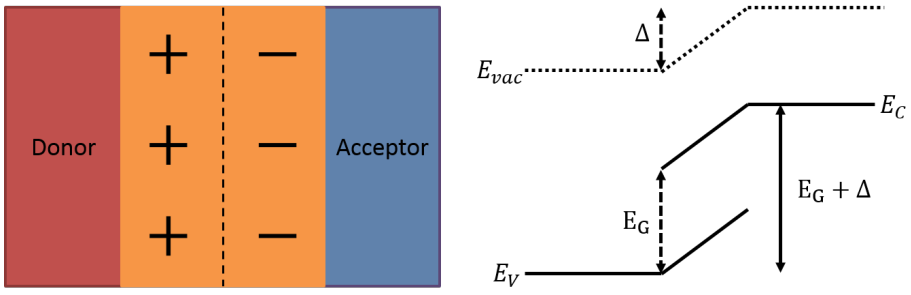

Figure 5.11: Schematic picture of the model for interfacial trap states. The interfacial layer has been cut in half and hole and electron trap states placed in the parts, hole traps are depicted with "+"and electron traps with "−". The trapped charges cause a dipole shift in the vacuum level in the absence of free charges. To the right the energy diagram of the interface is shown.

It has been proposed that the ICT states may act as trap states and cause trap-assisted recombination [28]. In this section, the possibility of trap-assisted recombination via trap states at the interface and the dipole shift cause by the trapped charges will be examined. In the model, the interfacial layer has been divided into two parts, the half closer to the donor phase and that closer to the acceptor. Hole trap states have been placed in the half closer to the donor and electron trap states in that closer to the acceptor. Trapped charges occupying these states cause a dipole shift Δ in the potential in the absence of free charges, the trap states and dipole shift are shown in Figure 5.11. The trap concentration N_t has been assumed equal for hole and electron traps.

Finding a way to study bimolecular and trap-assisted recombination separately is not straightforward, especially when the traps are only located in parts of the active layer. The light ideality factor n_{id} gives a measure of which recombination mechanism dominates at open circuit. The light ideality factor can be calculated from the following expression, assuming that $n \approx p$ and $n_{\text{trapped}} \approx p_{\text{trapped}}$:

$$eV_{oc} \approx E_g + \Delta - n_{id}kT \ln\left(\frac{C(\Delta)}{G}\right) \tag{5.6}$$

where C only depends on the dipole shift Δ. If $n_{id} = 2$ the recombination is purely trap-assisted and if $n_{id} = 1$ only bimolecular recombination occurs. By measuring V_{oc} as a function of G it is then possible to determine which recombination mechanism dominates in a given system. When the number of free charge carriers in the active layer is small, thermal excitations to the trap states will dominate over trapping of free charges. The number of trapped charges at a given time will then be proportional to the density of free charges and the recombination rate will be proportional to np, effectively behaving like bimolecular recombination.

At higher concentrations of free charge carriers, an approximate expression for V_{oc} can be derived when the recombination rates are given by the Langevin and SRH expressions. At open circuit, all generated charges recombine

$$G = R_L + R_{SRH}. \tag{5.7}$$

Neglecting all thermal excitations, the recombination rates can be approximated in the following way:

$$G = \left(C_n + C_p + N_t \frac{C_n C_p}{C_n n + C_p p}\right) np. \tag{5.8}$$

By noting that the product np is given by Equation 3.28 at V_{oc} and rearranging an expression for V_{oc} is obtained,

$$eV_{oc} = E_g + \Delta - kT\left(\ln(N_c N_v) + \ln\left(\frac{C_n + C_p + \frac{N_t C_n C_p}{C_n n + C_p p}}{G}\right)\right). \tag{5.9}$$

In the case of equal mobilities for electrons and holes $C_n = C_p$ and futher assuming that $n \approx p$ the expression can be simplified:

$$eV_{oc} \approx E_g + \Delta - kT\left(\ln(N_c N_v C_n) + \ln\left(\frac{2 + \frac{N_t}{2n}}{G}\right)\right). \tag{5.10}$$

An approximate expression for the electron concentration can be found from Equation 5.8 under the same assumptions

$$G \approx \left(2C_n + \frac{N_t C_n}{2n}\right) n^2. \tag{5.11}$$

The solution is given by:

$$n = -\frac{N_t}{8} + \sqrt{\frac{N_t^2}{64} + \frac{G}{2C_n}}. \tag{5.12}$$

This expression can be simplified assuming that $\frac{32G}{C_n N_t^2} << 1$. This assumption is true at up to fairly high generation rates, at which point bimolecular recombination is dominating and the term containing n is negligible. The electron concentration is then approximately given by:

$$n \approx \frac{2G}{C_n N_t}. \tag{5.13}$$

This way n can be expressed in terms of G and an expression for V_{oc} which is only dependent on G, T and N_t is obtained

$$eV_{oc} = E_g + \Delta - kT\left(\ln(N_c N_v C_n) + \ln\left(2G^{-1} + \frac{N_t^2 C_n}{4} G^{-2}\right)\right). \tag{5.14}$$

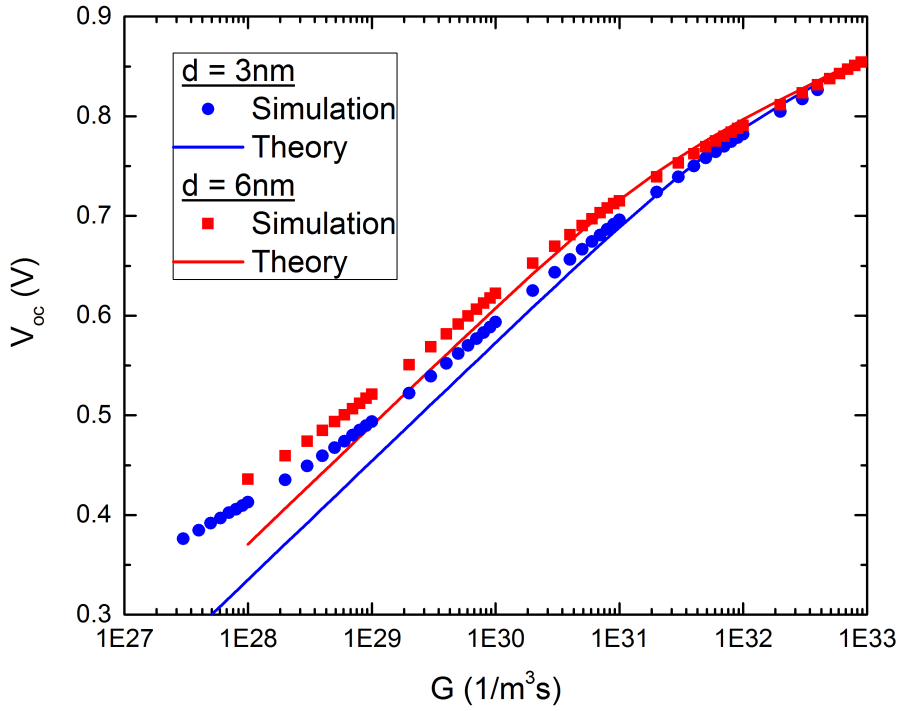

Figure 5.12: V_{oc} as a function of G for the basic finger structure with $d_{\text{interface}} =$ 3nm and 6nm. The ideality factor is given by the slope of the curve obtained when plotting V_{oc} as a function of $\ln(G)$. The theoretical value is given by equation 5.14 with $\Delta = 0$ eV.

At high generations the first term, proportional to G^{-1} will dominate and the value of the ideality factor,

$$n_{id} = \frac{e}{kT}\frac{dV_{oc}}{d(\ln(G))} = \frac{2G + \frac{N_t^2 C_n}{2}}{2G + \frac{N_t^2 C_n}{4}}, \tag{5.15}$$

will be close to 1. At lower concentration, the ideality factor will take on a value closer to 2 if the trap concentration is sufficiently high. At even low values for G the assumption that thermal excitations are negligible no longer holds and Equation 5.14 is no longer valid. In Figure 5.12, simulated values for two different widths of the interfacial layer are compared to V_{oc} obtained from Equation 5.14 and are seen to be in good agreement for sufficiently high values of G. In the simulations, a constant density of trap states with a depth of 0.3 eV has been assumed.

The theoretical expression is strongly dependent on Δ, but is seen to overlap well with simulation data when $\Delta = 0$ eV. The dipole shift in the case where $d_{\text{interface}} = 6$ nm and $N_t = 5 \cdot 10^{23}$ m^{-3} can be approximated to $\Delta \approx 0.2$ eV and should cause a significant shift in V_{oc} if present. The absence of a dipole shift may be due to the large density of free charges screening the field produced by the trapped charges.

5.3 Doping

Organic materials used in solar cells are typically intrinsically undoped. To alter transport properties of the active layer dopants can be added, thus introducing equilibrium carriers to the system. Organic materials are known to degrade as the active layer is easily oxidized, or in other words unintentionally doped.

The charge extraction by linearly increasing voltage (CELIV) method is a measurement technique used to study transport properties of thin film devices [29, 30]. In the measurement, a linearly increasing voltage pulse is applied to the sample and the transient response is observed. The voltage pulse is applied in the reverse direction and extracts equilibrium carriers while avoiding injection of additional charges. The current transient $j(t)$ can be divided into two parts, a constant geometric capacitive current j_0 and a time-dependent extraction current $\Delta j(t)$,

$$j(t) = j_0 + \Delta j(t). \tag{5.16}$$

The geometrical capacitive response is simply given by

$$j_0 = \frac{\epsilon\epsilon_0 A}{d} \tag{5.17}$$

where $A = U_{max}/t_{pulse}$ is the voltage rise speed. The length of the pulse can be tuned to obtain various transport properties in different regimes.

If the sample contains a large concentrations of dopants N_{dopant}, a region depleted of free charges exists at one of the electrodes. The width of the depletion region $w(t)$ is given by the following expression for long pulses, when the maximum value of $j(t)$ is reached in at beginning of the pulse [31]:

$$w(t) = \sqrt{\frac{2\epsilon\epsilon_0(At + U_{bi} - \frac{kT}{e})}{eN_{\text{dopant}}}}. \tag{5.18}$$

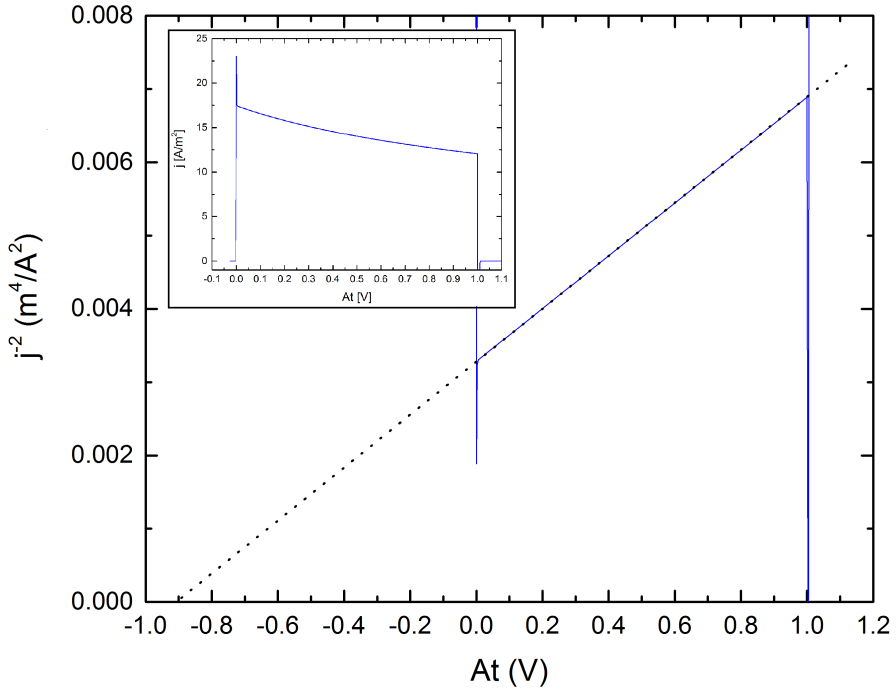

Figure 5.13: Simulated CELIV transient for the morphology shown in Figure 4.4 with a doping concentration of $N_p = 2 \cdot 10^{-18}\text{cm}^{-2}$ in the donor and interfacial layer and $A = 1\text{V}/100\mu\text{s}$. The linear relation between j^{-2} and At can be used to calculate the doping concentrations. The built-in potential U_{bi} is obtained from the extrapolated dotted line. The inset shows j as a function of At.

In this case the current transient becomes purely capacitive as long as $w(t) < d$ and is given by:

$$j(t) = \frac{\epsilon\epsilon_0 A}{w(t)} = \sqrt{\frac{eN_{\text{dopant}}\epsilon\epsilon_0}{2}} \frac{A}{\sqrt{At + U_{bi} - \frac{kT}{e}}}. \tag{5.19}$$

By plotting $j(t)^{-2}$ as a function of At, both N_{dopant} and U_{bi} can be determined from the same measurement. The derivation above is done for the one dimensional case with a uniformly distributed concentration of dopants.

By considering a case where dopants are only found in one of the phases, we can ensure that the doping CELIV approach is viable even though the dopants are not uniformly distributed on a nanoscale. The basic finger structure for the active layer with a doping concentration of $N_p = 2 \cdot 10^{18}$ cm^{-3} for the donor and interfacial layer has been considered. The current transient for $A = 1\text{V}/100\mu\text{s}$ is shown in Figure 5.13. The linear relation between j^{-2} and At can be seen, as well as $U_{bi} = 0.9$ V from extrapolation. A doping concentration of $N_p = 1.15 \cdot 10^{18}$ cm^{-2} was calculated from slope.

If the non-uniform distribution on a nanometer scale is not important an, effective doping concentration can be calculated. The effective concentration is simply the concentration obtained if the dopants were uniformly spread over the whole active layer. The effective doping concentration N_p^{eff} is then given by

$$N_p^{\text{eff}} = \frac{a_{\text{dopants}}}{a_{\text{AL}}} N_p \tag{5.20}$$

where $\frac{a_{\text{dopants}}}{a_{\text{AL}}}$ is the ratio between the area where dopants are found and the total active layer area. If N_p^{eff} is calculated for the simulated case a value of $1.15{\cdot}10^{18}$ cm^{-2} is obtained, exactly equal to that calculated from the CELIV transient.

Chapter 6

Conclusions and Future Work

A flexible two-dimensional drift-diffusion model has been developed for organic bulk heterojunction solar cells. The two-dimensional model makes it possible to consider the effects of the morphology of the active layer, in contrast to a one-dimensional model. A one-dimensional model can also be readily obtained by increasing the interfacial layer thickness until it makes up the entire active layer. Unfortunately, the two-dimensional model is significantly more time consuming than the one-dimensional model.

The focus of the presented simulation data was on clarifying the role of recombination dynamics occuring at the interface between the donor and acceptor. A comparison to the commonly used one-dimensional effective semiconductor model has been presented. In some cases it is possible to reproduce the results of the two-dimensional model in one-dimensional one by using effective parameters. When possible, such effective parameters have been derived and shown to reproduce the results of the two-dimensional model.

Recombination mechanisms in organic materials are still not well understood and the model suffers from this fact. However, simulations like the one developed in this work may be of great importance when it comes to resolving these issues. For example, it is unclear whether the Langevin and SRH expressions are well suited for describing recombination when the separate phases are considered. An in-depth study of the probability of charge carriers meeting at the interface of the materials would be beneficial.

Minor errors in the recombination rate in the model may arise due to the use of charge carrier concentrations instead of discrete charges. As a result of this, fractions of charges are allowed to recombine and the strenght of coulomb interactions may be underestimated. Another, in some cases larger, error in the recombination rate is also present in the model. The intermediate recombination step of a bound electron-hole pair that may dissociate again [25] is not included. If the probability of re-dissociation is large, the recombination rate will be severely overestimated.

The simple model of interfacial trap states presented in this work gives a rough estimate of the magnitude of recombination occurring at these. An exponential or Gaussian trap distribution should replace the single trap level considered in this model in order to make it more realistic. The transient behavior of trapped charges may also prove to be of great interest when simulating transient experiments.

Chapter 7

Swedish Summary
Svensk sammanfattning: Tvådimensionell drift–diffusion-simulering av organiska solceller

Introduktion

Organiska solceller uppnår ännu en relativt låg verkningsgrad jämfört med oorganiska sådanna. Organiska material uppvisar en stor grad av oordning förorsakad av de svaga van der Waal-krafter som binder samman molekylerna. Denna underliggande oordning leder till ineffektiv laddningstransport och svårigheter att erhålla önskad morfologi för det aktiva lagret. En annan orsak till den låga verkningsgraden är starkt bundna excitoner som måste separeras, till exempel vid gränsytan mellan två material. Bulkgränsytesolceller är en typ av solceller där ett elektronaccepterande och elektrondonerande material, förkortade acceptor och donor har blandats för att uppnå effektiv laddningsseparation.

I det här arbetet har en tvådimensionell drift–diffusion-modell utvecklats. De två rymddimensionerna är speciellt viktiga i solceller av bulkgränsytetyp, då processer som sker vid gränsytan är avgörande. Målet med modellen är att få en närmare inblick i hur olika förlustmekanismer påverkar verkningsgraden hos organiska solceller.

Teori

Den oordning som förekommer bland organiska halvledare kan beskrivas som en distribution av lokaliserade energitillstånd. Tillståndstätheten, som vanligtvis antas vara gaussisk [2], består av energitillstånd som är lokaliserade på de enskilda molekylerna i den organiska halvledaren. Transport i organiska material kan beskrivas som en serie av termiskt aktiverade hopp mellan lokaliserade tillstånd [3]. Med hjälp av Monte Carlo-simuleringar har ett uttryck för mobiliteten μ erhållits [2],

$$\mu(F,T) = \mu_0 \exp\left[-\left(\frac{2}{3}\frac{\sigma}{kT}\right)\right] \exp\left[CF^{1/2}\left(\left(\frac{\sigma}{kT}\right)^2 - \Sigma^2\right)\right] \tag{7.1}$$

där μ_0 är en materialberoende parameter och σ är bredden på den Gaussiska tillståndstätheten. De två empiriska parametrarna, Σ och C, i uttrycket kan bestämmas genom anpassning till experimentella data. Vid rumstemperatur är fältberoendet svagt och så länge temperaturskillnader inte förekommer kan mobiliteten antas vara konstant.

I en enkel modell antas fria elektroner befinna sig vid en energinivå E_C och fria hål vid E_V. De effektiva tillståndstätheter givna av N_C och N_V beskriver koncentrationen av tillstånd för nivåerna . Denna förenkling av energistrukturen leder till att termiskt exciterade laddningskoncentrationer enkelt kan beräknas med hjälp av Fermi-statistik. Koncentrationerna av fria elektroner n och hål p ges då av

$$\begin{aligned} n &= N_{\mathrm{C}} \exp\left(\frac{E_F - E_{\mathrm{C}}}{kT}\right) \\ p &= N_{\mathrm{V}} \exp\left(\frac{E_{\mathrm{V}} - E_F}{kT}\right) \end{aligned} \tag{7.2}$$

vid termodynamisk jämvikt. Ferminivån E_F för en halvledare vid termodynamisk jämvikt ligger i mitten av energigapet $E_g = E_{\mathrm{C}} - E_{\mathrm{V}}$. Vid rumstemperatur är kT mycket mindre än E_g och därför förekommer endast väldigt få termiskt exciterade laddningsbärare i en halvledare. Om halvledaren förses med fria laddningsbärare genom fotogeneration beskriver ekvation 7.2 inte längre laddningskoncentrationerna eftersom termodynamisk jämvikt inte längre råder.

Laddningsbärare uppnår snabbt separata jämvikter och skilda kvasi-Ferminivåer för fria elektroner E_F^n och hål E_F^p kan användas för att beskriva dessa. Då E_F ersätts med kvasi-Ferminivåer gäller ekvation 7.2 även i detta fall. Produkten av laddningskoncentrationer np kan då också beräknas,

$$np = N_{\mathrm{C}} N_{\mathrm{V}} \exp\left(\frac{E_F^n - E_F^p}{kT}\right) \exp\left(-\frac{E_g}{kT}\right). \tag{7.3}$$

Kvasi-Ferminivåerna kan även delas in i kemisk och elektrisk potential, ξ och ψ:

$$\begin{aligned} E_F^n &= \xi_n - e\psi \\ E_F^p &= \xi_p + e\psi. \end{aligned} \tag{7.4}$$

Laddningstransporten i en halvledare sker genom en kombination av drift och diffusion. En driftström $\bar{j}_{\mathrm{drift}}$ uppstår då laddningar rör sig under inverkan av ett elektriskt fält $\bar{F}$. Driftströmmen ges av

$$\bar{j}_{\mathrm{drift}} = -e\bar{F}(n\mu_n + p\mu_p) \tag{7.5}$$

där $\mu_{n,p}$ är mobiliteten för elektroner och hål. Diffusion uppstår då gradienter av laddningskoncentrationer förekommer. Genom att tillämpa Einsteinrelationen erhålls följande uttryck för diffusionsströmmen $\bar{j}_{\mathrm{diff}}$:

$$\bar{j}_{\mathrm{diff}} = kT(\mu_n \nabla n - \mu_p \nabla p). \tag{7.6}$$

Den totala strömmen kan även skrivas som funktioner av kvasi-Ferminivåerna, den separata elektron- och hålströmmen ges då av

$$\begin{aligned} \bar{j}_n &= n\mu_n \nabla E_F^n \\ \bar{j}_p &= p\mu_p \nabla E_F^p. \end{aligned} \tag{7.7}$$

Ekvationerna illustrerar energinivåernas samband med strömmen och visar den centrala roll dessa spelar. Poissons ekvation

$$\nabla^2\psi = \frac{n-p}{\epsilon\epsilon_0} \tag{7.8}$$

och kontinuitetsekvationen

$$\nabla \cdot \bar{J} = \frac{\partial}{\partial t}(n-p) \tag{7.9}$$

kan utnyttjas för att lösa transportproblemet då strömmen ges av $\bar{J} = \bar{j}_n + \bar{j}_p$.

Rekombinationshastigheten R beskriver hur ofta rekombination av ett par av laddningsbärare inträffar. Olika typer av rekombination existerar men endast de två vanligaste formerna har beaktats i det här arbetet. Langevins rekombinationsteori beskriver sannolikheten att två fria laddningsbärare möts och ger följande uttryck för rekombinationshastigheten [12]:

$$R_L = np\frac{e}{\epsilon\epsilon_0}(\mu_n + \mu_p). \tag{7.10}$$

Förutom fria laddningar kan även laddningar i fällor bidra till rekombinationen. Ett motsvarande uttryck för rekombination av en fri laddning och en laddning i en fälla ges av Shockley-Read-Hall-rekombinationshastigheten R_{SRH} [15]. Rekombinationshastigheten beror av koncentrationen av fällor N_t och koncentrationen av termiska excitationer till fällorna $n_{\mathrm{term}}, p_{\mathrm{term}}$. Rekombinationshastigheten ges av

$$R_{SRH} = N_t C_n C_p \frac{np}{C_n(n+n_{\mathrm{term}}) + C_p(p+p_{\mathrm{term}})} \tag{7.11}$$

där $C_{n,p}$ är faktorer motsvarande de i Langevin-uttrycket,

$$C_{n,p} = \mu_{n,p}\frac{e}{\epsilon\epsilon_0}. \tag{7.12}$$

De två uttrycken för rekombinationshastigheten, speciellt Langevinrekombinationen, har visats ge felaktiga resultat i en del organiska system [13, 14].

Modell

Modellen som har utvecklats tillämpar den teori som har presenterats ovan för att beräkna koncentrationer av fria laddningsbärare och den elektriska potentialen i det aktiva lagret. Ett gränsskikt har implementerats för att beskriva gränsytan mellan donorn och acceptorn. Gränsskiktet har acceptorns elektrontransportegenskaper och donorns håltransportegenskaper, såväl som deras respektive energinivåer. Excitoner har utelämnats från modellen och istället sker en effektiv generation av fria laddningsbärare i gränsskiktet. Elektroner i gränsskiktet diffunderar endast in i den rena acceptorfasen, eftersom en stor energibarriär måste övervinnas för att komma in i donorn. På motsvarande sätt diffunderar hål in i den rena donorfasen.

Morfologin för det aktiva lagret har antagits ha en fingerstruktur som är optimerad för laddningstransport och separation av excitoner. En schematisk bild av strukturen visas i figur 7.1. Energinivåerna i modellen har tagits som de för P3HT:PCBM, som uppvisar en struktur lika den ovan nämnda [11].

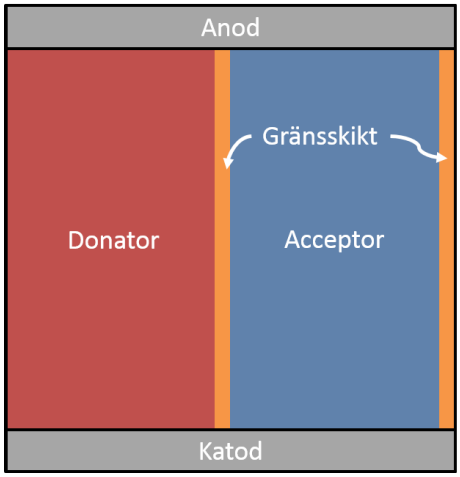

Figur 7.1: Schematisk bild av den morfologi som har använts i modellen. De två rena faserna är separerade av ett gränsskikt där generation och rekombination sker. Strukturen upprepas i sidled, implementerat med hjälp av periodiska randvillkor.

Ekvationssystemet som utgörs av Poissons ekvation och kontinuitetsekvationerna för elektroner och hål löses numeriskt i simuleringen. För att finna en numerisk lösning delas det aktiva lagret in i ett antal diskreta punkter, vartefter transportproblemet kan lösas för dessa. I x-led delas lagret in i N_x punkter, separerade av avståndet h. På motsvarande sätt delas y-ledet in i N_y punkter och avståndet mellan två brevid varandra liggande punkter $x_{i,j}$ och $x_{i,j+1}$ ges av k. Derivator av första och andra ordning för potentialen kan approximeras på följande sätt:

$$\frac{\partial \psi}{\partial x}\Big|_{i,j} = \frac{\psi_{i+1/2,j} - \psi_{i-1/2,j}}{h} \tag{7.13}$$

$$\frac{\partial^2 \psi}{\partial x^2}\Big|_{i,j} = \frac{\psi_{i+1,j} - 2\psi_{i,j} + \psi_{i-1,j}}{h^2}. \tag{7.14}$$

Strömtäthetens derivator kan uppskattas på motsvarande sätt. Laddningskoncentrationer har ofta exponentiella avståndsberoenden; därför har en uppskattning föreslagen av Scharfetter och Gummel [19] utnyttjats

$$\frac{\partial n}{\partial x}\Big|_{i+1/2,j} = \frac{\psi_{i+i,j} - \psi_{i,j}}{exp(\frac{\psi_{i+1,j} - \psi_{i,j}}{2}) - exp(\frac{\psi_{i,j} - \psi_{i+1,j}}{2})} \cdot \frac{n_{i+1,j} - n_{i,j}}{h}. \tag{7.15}$$

Därtill måste tidsderivator diskretiseras. Detta har gjorts på följande sätt

$$\frac{\partial n}{\partial t}\Big|_{i,j,m+1} = \frac{n_{i,j,m+1} - n_{i,j,m}}{\Delta t} \tag{7.16}$$

där Δt är tidsskillnaden mellan två på varandra följande tidpunkter. Dessa approximationer är endast godtagbara då h, k och Δt är små. Fullständiga uttryck för de diskreta versionerna av Poissons ekvation och kontinuitetsekvationerna hittas i appendix A, men notera att en normalisering som eliminerar konstanter har gjorts.

För att lösa de erhållna diskreta ekvationerna har en iterativ metod kallad SOR (engelska: *Successive Over-Relaxation*) tillämpats. Metoden erhålls genom matrisfaktorisering men kan uttryckas för enskilda termer i ekvationssystemet. Ekvationssystemen kan skrivas i matrisform,

$$\bar{\bar{A}}\bar{x} = \bar{b}, \tag{7.17}$$

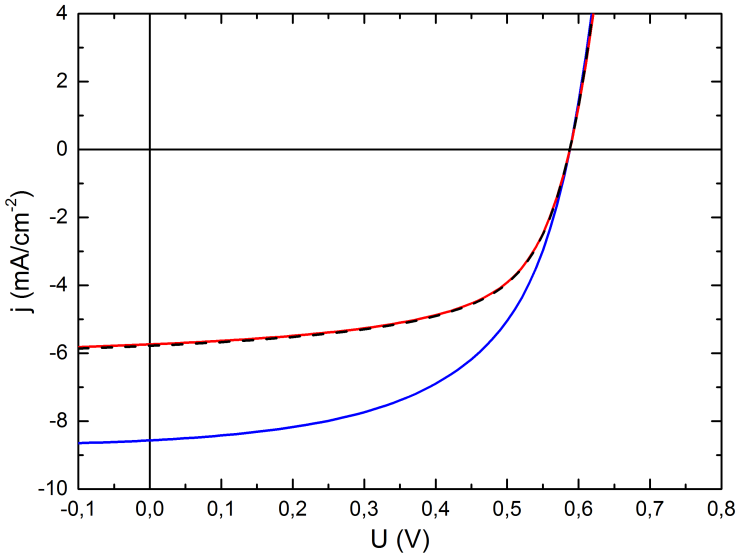

Figur 7.2: J–U-kurva för fallet med en acceptordomän i den rena donorfasen. Domänen är till en början helt isolerad, givet av den röda linjen. Därefter flyttas domänen så att den är i kontakt med gränsskiktet mellan faserna och den blåa linjen erhålls. Den streckade svarta linjen visar strömmen för den ursprungliga strukturen då antalet laddningar som genereras vid gränsskiktet är detsamma som i de tidigare fallen.

där $\bar{x}$ innehåller de okända variablerna. Då ges lösningen för iterationssteg $k+1$ och element u enligt

$$x_u^{k+1} = (1-\omega)x_u^k + \frac{\omega}{a_{uu}}(b_u - \sum_{v<u} a_{uv}x_v^{k+1} - \sum_{v>u} a_{uv}x_v^k), u = 1, 2, ..., N. \qquad (7.18)$$

där ω är en relaxationsparameter och a_{uv} är matriselement i $\bar{\bar{A}}$. Parametern bestämmer konvergenshastigheten, men att bestämma det optimala värdet för ω är inte elementärt.

Resultat

Modellen visas reproducera kända teoretiska värden för laddningskoncentrationer, kvasi-Ferminivåer och diodströmmen, se kapitel 5.1. Därmed kan mer vikt fästas vid övriga simuleringsdata.

Isolerade domäner av en fas, helt omgiven av den andra fasen förekommer ofta i bulkgränsytematerial. För att simulera dessa placerades en acceptordomän mitt i den rena donorfasen. Ett andra fall där domänen flyttades så att den var i kontakt med gränsskiktet simulerades för att de två skulle kunna jämföras. J–U-kurvor för de två fallen visas i figur 7.2. En stor minskning i fotoströmmen observeras för fallet med den isolerade domänen, trots att antalet genererade laddningar var lika i båda fallen. Då samma antal laddningar genereras vid gränsskiktet i den ursprungliga strukturen erhålls nästan samma resultat som i fallet med en isolerad domän. De slutsatser som kan dras är att alla laddningsbärare som genererades vid den isolerade domänen rekombinerar, vilket ses som överlappande J–U-kurvor för fallen med

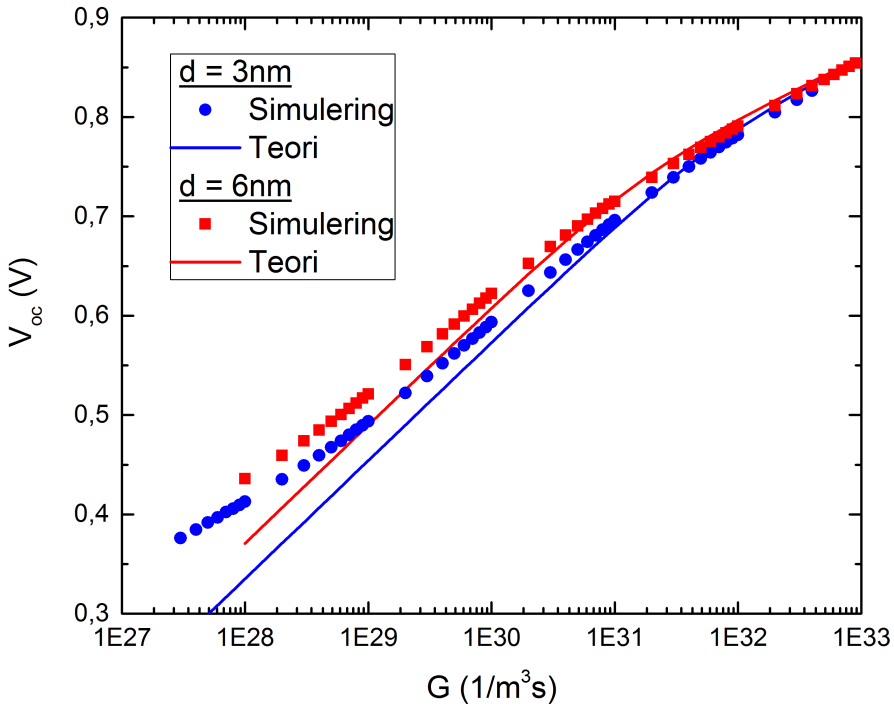

Figur 7.3: V_{oc} ritat som funktion av G. De heldragna linjerna visar det teoretiska värdet för V_{oc} givet i ekvation 7.21. Idealitetsfaktorn fås från lutningen på kurvan då V_{oc} ritas som en funktion av $\ln(G)$.

och utan isolerad domän. Därtill verkar domänen inte ha en märkbar inverkan på laddningstransporten vid låga värden för den applicerade spänningen.

ICT-teorin (från engelska: *Integer charge transfer*) har förutspått att elektroner spontant överförs från donatorn till acceptorn och fångas av fällor vid gränsytan, kallade ICT-tillstånd [27]. De fångade laddningarna förorsakar en dipol över gränsytan och leder till en ökad rekombination [28]. Dipolen ses som en potentialskillnad Δ i energinivåerna. Storleksordningen på rekombinationen via fällorna kan undersökas med hjälp av idealitetsfaktorn n_{id}. Idealitetsfaktorn kan bestämmas ur följande uttryck

$$eV_{oc} \approx E_g + \Delta - n_{id}kT \ln\left(\frac{C(\Delta)}{G}\right), \tag{7.19}$$

där V_{oc} är spänningsskillnaden mellan elektroderna då ingen ström flyter genom solcellen och $C(\Delta)$ endast beror av ytskiktsdipolen. Då n_{id} är lika med ett är den rekombination som sker effektivt bimolekylär, men om värdet för n_{id} istället är närmare två dominerar rekombination via fällor. Två fall med olika tjocklekar för gränsskiktet undersöktes genom att beräkna V_{oc} för flera storleksordningars variationer av G.

En mer noggrann härledning för idealitetsfaktorn gjordes för analysen av resultaten, se kapitel 5.2.2. Ett approximativt uttryck för n_{id} ges av

$$n_{id} = \frac{e}{kT}\frac{dV_{oc}}{d(\ln(G))} = \frac{2G + \frac{N_t^2 C_n}{2}}{2G + \frac{N_t^2 C_n}{4}} \tag{7.20}$$

där N_t är koncentrationen av fällor. Ett uttryck för V_{oc} erhölls

$$eV_{oc} = E_g + \Delta - kT\left(\ln(N_c N_v C_n) + \ln\left(2G^{-1} + \frac{N_t^2 C_n}{4} G^{-2}\right)\right), \tag{7.21}$$

som överrensstämmer väl med resultaten från simuleringen. Resultaten presenteras i figur 7.3. I båda fallen erhölls $\Delta = 0$ eV, även om storleksordningen för denna borde vara ungefär 0.2 eV.

Diskussion

En flexibel tvådimensionell drift–diffusion-simulering har utvecklats och visats reproducera kända transportegenskaper. Modellen har använts för att studera processer som inträffar vid gränsytan mellan de två material som utgör det aktiva lagret i en organisk solcell av bulkgränsytetyp. Effektiva parametrar som kan användas i en endimensionell modell har även presenterats då detta har varit möjligt.

Bibliography

[1] R. A. J. Janssen and J. Nelson, Factors limiting device efficiency in organic photovoltaics, Advanced Materials **25**, 1847 (2013).

[2] H. Bässler, Charge transport in disordered organic photoconductors a monte carlo simulation study, physica status solidi (b) **175**, 15 (1993).

[3] R. A. Marcus, Electron transfer reactions in chemistry. theory and experiment, Reviews of Modern Physics **65**, 599 (1993).

[4] A. Miller and E. Abrahams, Impurity conduction at low concentrations, Physical Review **120**, 745 (1960).

[5] A. J. Mozer, N. S. Sariciftci, A. Pivrikas, R. Österbacka, G. Juška, L. Brassat, and H. Bässler, Charge carrier mobility in regioregular poly(3-hexylthiophene) probed by transient conductivity techniques: A comparative study, Physical Review B **71**, 035214 (2005).

[6] P. Schilinsky, Simulation of light intensity dependent current characteristics of polymer solar cells, Journal of Applied Physics **95**, 2816 (2004).

[7] S. van Bavel, E. Sourty, G. de With, K. Frolic, and J. Loos, Relation between photoactive layer thickness, 3d morphology, and device performance in p3ht/pcbm bulk-heterojunction solar cells, Macromolecules **42**, 7396 (2009).

[8] G. Chamberlain, Organic solar cells: A review, Solar Cells **8**, 47 (1983).

[9] C. W. Tang, Two-layer organic photovoltaic cell, Applied Physics Letters **48** (1986).

[10] G. A. Buxton and N. Clarke, Predicting structure and property relations in polymeric photovoltaic devices, Physical Review B **74** (2006).

[11] J. S. Moon, J. K. Lee, S. Cho, J. Byun, and A. J. Heeger, "Columnlike" structure of the Cross-Sectional morphology of bulk heterojunction materials, Nano Letters **9**, 230 (2009).

[12] M. Langevin, Recombinaison et mobilités des ions dans les gaz, Annales de chimie et de physique **28**, 433 (1903).

[13] G. Juška, K. Arlauskas, J. Stuchlik, and R. Österbacka, Non-langevin bimolecular recombination in low-mobility materials, Journal of Non-Crystalline Solids **352**, 1167 (2006).

[14] C. Groves and N. C. Greenham, Bimolecular recombination in polymer electronic devices, Physical Review B **78**, 155205 (2008).

[15] W. Shockley and W. T. Read, Statistics of the recombinations of holes and electrons, Physical Review **87**, 835 (1952).

[16] J. Nelson, *The Physics of Solar Cells* (Imperial College, UK, 2003).

[17] M. A. Lampert and P. Mark, *Current Injection in Solids* (Academic Press, New York, 1970).

[18] S. Selberherr, *Analysis and Simulation of Semiconductor Devices* (Springer-Verlag, New York, NY, USA, 1984).

[19] D. Scharfetter and H. Gummel, Large-signal analysis of a silicon read diode oscillator, IEEE Transactions on Electron Devices **16**, 64 (1969).

[20] D. Young, Iterative methods for solving partial difference equations of elliptic type, Transactions of the American Mathematical Society **76**, 92 (1954).

[21] Y. Saad, *Iterative Methods for Sparse Linear Systems* (Society for Industrial and Applied Mathematics, 2003).

[22] F. F. Stelzl and U. Würfel, Modeling the influence of doping on the performance of bulk heterojunction organic solar cells: One-dimensional effective semiconductor versus two-dimensional donor/acceptor model, Physical Review B **86** (2012).

[23] P. E. Shaw, A. Ruseckas, and I. D. W. Samuel, Exciton diffusion measurements in poly(3-hexylthiophene), Advanced Materials **20**, 3516 (2008).

[24] A. Huijser, T. J. Savenije, A. Shalav, and L. D. A. Siebbeles, An experimental study on the molecular organization and exciton diffusion in a bilayer of a porphyrin and poly(3-hexylthiophene), Journal of Applied Physics **104** (2008).

[25] L. J. A. Koster, V. D. Mihailetchi, and P. W. M. Blom, Bimolecular recombination in polymer/fullerene bulk heterojunction solar cells, Applied Physics Letters **88**, 052104 (2006).

[26] C. Deibel, A. Wagenpfahl, and V. Dyakonov, Origin of reduced polaron recombination in organic semiconductor devices, Physical Review B **80**, 075203 (2009).

[27] S. Braun, W. R. Salaneck, and M. Fahlman, Energy-level alignment at organic/metal and organic/organic interfaces, Advanced Materials **21**, 1450 (2009).

[28] Q. Bao, O. Sandberg, D. Dagnelund, S. Sandén, S. Braun, H. Aarnio, X. Liu, W. M. Chen, R. Österbacka, and M. Fahlman, Trap-Assisted recombination via integer charge transfer states in organic bulk heterojunction photovoltaics, Advanced Functional Materials **24**, 6309 (2014).

[29] G. Juška, K. Arlauskas, M. Viliūnas, K. Genevičius, R. Österbacka, and H. Stubb, Charge transport in π-conjugated polymers from extraction current transients, Physical Review B **62**, R16235 (2000).

[30] G. Juška, K. Genevičius, K. Arlauskas, R. Österbacka, and H. Stubb, Charge transport at low electric fields in π-conjugated polymers, Physical Review B **65**, 233208 (2002).

[31] O. J. Sandberg, M. Nyman, and R. Österbacka, Direct determination of doping concentration and built-in voltage from extraction current transients, Organic Electronics **15**, 3413 (2014).

Appendix A

Appendix I

In this appendix, the full expressions for the discretized two-dimensional Poisson and continuity equations are given, the expression are also found in [18]. The normalization given in Table 4.1 has been used to eliminate constants from the equations. Note that the distance between points in a given direction have been taken to be constant. The discrete Poisson equation is given by

$$\begin{aligned}\left(\psi'_{i,j-1,m+1}+\psi'_{i,j+1,m+1}\right)\cdot\frac{h}{k}+\left(\psi'_{i-1,j,m+1}+\psi'_{i+1,j,m+1}\right)\cdot\frac{k}{h}\\ -2\psi'_{i,j,m+1}\cdot\left(\frac{h}{k}+\frac{k}{h}\right)=\left(n'_{i,j,m+1}-p'_{i,j,m+1}+Q'_{i,j,m+1}\right)\cdot hk\end{aligned}\quad\text{(A.1)}$$

where $Q'_{i,j,m+1}$ describes stationary charges such as dopants and trapped charges.

The continuity equations are given below. The solution to the continuity equation contains Bernoulli function $B(\Delta\psi)$ which is given by:

$$B(\Delta\psi)=\frac{\Delta\psi}{\exp(\Delta\psi)-1}. \quad\text{(A.2)}$$

For small potential differences $\Delta\psi << 1$ the Bernoulli function can be approximated as $B(\Delta\psi)\approx 1$.

$$
\begin{aligned}
& n'_{i,j-1,m+1} \cdot \mu'^{n}_{i,j-1/2,m+1} \cdot B(\psi'_{i,j-1,m+1} - \psi'_{i,j,m+1}) \cdot \frac{h}{k} \\
+ \; & n'_{i-1,j,m+1} \cdot \mu'^{n}_{i-1/2,j,m+1} \cdot B(\psi'_{i-1,j,m+1} - \psi'_{i,j,m+1}) \cdot \frac{k}{h} \\
+ \; & n'_{i,j+1,m+1} \cdot \mu'^{n}_{i,j+1/2,m+1} \cdot B(\psi'_{i,j+1,m+1} - \psi'_{i,j,m+1}) \cdot \frac{h}{k} \\
+ \; & n'_{i+1,j,m+1} \cdot \mu'^{n}_{i+1/2,j,m+1} \cdot B(\psi'_{i+1,j,m+1} - \psi'_{i,j,m+1}) \cdot \frac{k}{h} \\
- \; & n'_{i,j,m+1} \cdot \big(\mu'^{n}_{i,j-1/2,m+1} \cdot B(\psi'_{i,j,m+1} - \psi'_{i,j-1,m+1}) \cdot \frac{h}{k} \\
& \qquad + \mu'^{n}_{i-1/2,j,m+1} \cdot B(\psi'_{i,j,m+1} - \psi'_{i-1,j,m+1}) \cdot \frac{k}{h} \\
& \qquad + \mu'^{n}_{i,j+1/2,m+1} \cdot B(\psi'_{i,j,m+1} - \psi'_{i,j+1,m+1}) \cdot \frac{h}{k} \\
& \qquad + \mu'^{n}_{i+1/2,j,m+1} \cdot B(\psi'_{i,j,m+1} - \psi'_{i+1,j,m+1}) \cdot \frac{k}{h} \\
& \qquad + \frac{hk}{\Delta t}\big) \\
= \; & \big(R'_{i,j,m+1} - G_{i,j,m+1} - \frac{n'_{i,j,m}}{\Delta t}\big) \cdot hk
\end{aligned}
\tag{A.3}
$$

$$
\begin{aligned}
& p'_{i,j-1,m+1} \cdot \mu'^{p}_{i,j-1/2,m+1} \cdot B(\psi'_{i,j,m+1} - \psi'_{i,j-1,m+1}) \cdot \frac{h}{k} \\
+ \; & p'_{i-1,j,m+1} \cdot \mu'^{p}_{i-1/2,j,m+1} \cdot B(\psi'_{i,j,m+1} - \psi'_{i-1,j,m+1}) \cdot \frac{k}{h} \\
+ \; & p'_{i,j+1,m+1} \cdot \mu'^{p}_{i,j+1/2,m+1} \cdot B(\psi'_{i,j,m+1} - \psi'_{i,j+1,m+1}) \cdot \frac{h}{k} \\
+ \; & p'_{i+1,j,m+1} \cdot \mu'^{p}_{i+1/2,j,m+1} \cdot B(\psi'_{i,j,m+1} - \psi'_{i+1,j,m+1}) \cdot \frac{k}{h} \\
- \; & p'_{i,j,m+1} \cdot \big(\mu'^{p}_{i,j-1/2,m+1} \cdot B(\psi'_{i,j-1,m+1} - \psi'_{i,j,m+1}) \cdot \frac{h}{k} \\
& \qquad + \mu'^{p}_{i-1/2,j,m+1} \cdot B(\psi'_{i-1,j,m+1} - \psi'_{i,j,m+1}) \cdot \frac{k}{h} \\
& \qquad + \mu'^{p}_{i,j+1/2,m+1} \cdot B(\psi'_{i,j+1,m+1} - \psi'_{i,j,m+1}) \cdot \frac{h}{k} \\
& \qquad + \mu'^{p}_{i+1/2,j,m+1} \cdot B(\psi'_{i+1,j,m+1} - \psi'_{i,j,m+1}) \cdot \frac{k}{h} \\
& \qquad + \frac{hk}{\Delta t}\big) \\
= \; & \big(R'_{i,j,m+1} - G'_{i,j,m+1} - \frac{n'_{i,j,m}}{\Delta t}\big) \cdot hk
\end{aligned}
\tag{A.4}
$$